



1 **The new Kr-86 excess ice core proxy for synoptic activity: West Antarctic**
2 **storminess possibly linked to ITCZ movement through the last deglaciation**

3 Christo Buizert¹, Sarah Shackleton², Jeffrey P. Severinghaus², William H. G. Roberts³, Alan Seltzer^{2,4},
4 Bernhard Bereiter⁵, Kenji Kawamura⁶, Daniel Baggenstos⁵, Anaïs J. Orsi^{7,8}, Ikumi Oyabu⁶,
5 Benjamin Birner², Jacob D. Morgan², Edward J. Brook¹, David M. Etheridge^{9,10}, David Thornton⁹,
6 Nancy Bertler^{11,12}, Rebecca L. Pyne¹¹, Robert Mulvaney¹³, Ellen Mosley-Thompson¹⁴, Peter D. Neff^{15,16},
7 and Vasilii V. Petrenko¹⁶

8 ¹College of Earth, Ocean and Atmospheric Sciences, Oregon State University, Corvallis, OR 97331, USA

9 ²Scripps Institution of Oceanography, University of California San Diego, La Jolla, CA 92093, USA

10 ³Geography and Environmental Sciences, Northumbria University, Newcastle, UK and BRIDGE, School
11 of Geographical Sciences, University of Bristol, Bristol, UK

12 ⁴Marine Chemistry and Geochemistry Department, Woods Hole Oceanographic Institution, Woods Hole,
13 MA 02543, USA

14 ⁵Climate and Environmental Physics, Physics Institute, and Oeschger Center for Climate Research,
15 University of Bern, 3012, Bern, Switzerland

16 ⁶National Institute for Polar Research, 10-3 Midori-cho, Tachikawa, Tokyo 190-8518, Japan

17 ⁷Laboratoire des Sciences du Climat et de l'Environnement, LSCE/IPSL, CEA-CNRS-UVSQ, Université
18 Paris-Saclay, l'Orme des merisiers, Gif-sur-Yvette, France

19 ⁸Earth, Ocean and Atmospheric Sciences Department, The University of British Columbia, Vancouver, BC
20 V6T 1Z4, Canada

21 ⁹CSIRO Oceans and Atmosphere, PMB 1, Aspendale, Victoria 3195, Australia

22 ¹⁰Australian Antarctic Program Partnership, Institute for Marine & Antarctic Studies, University of
23 Tasmania, Hobart, Tasmania 7004, Australia

24 ¹¹Antarctic Research Centre, Victoria University of Wellington, Wellington, 6012, New Zealand

25 ¹²GNS Science, Lower Hut 5010, New Zealand

26 ¹³British Antarctic Survey, National Environment Research Council, Cambridge CB3 0ET, UK

27 ¹⁴Byrd Polar and Climate Research Center, The Ohio State University, Columbus, OH 43210, USA

28 ¹⁵Department of Soil, Water, and Climate, University of Minnesota, Saint Paul, MN 55108, USA

29 ¹⁶Department of Earth and Environmental Sciences, University of Rochester, Rochester, NY 14627, USA

30

31 *Correspondence to:* Christo Buizert (christo.buizert@oregonstate.edu)



32 **Abstract**

33 Here we present a newly developed ice core gas-phase proxy that directly samples a component of the
34 large-scale atmospheric circulation: synoptic-scale pressure variability. Surface pressure variability weakly
35 disrupts gravitational isotopic settling in the firn layer, which is recorded in krypton-86 excess ($^{86}\text{Kr}_{\text{xs}}$). We
36 validate $^{86}\text{Kr}_{\text{xs}}$ using late Holocene ice samples from eleven Antarctic and one Greenland ice core that
37 collectively represent a wide range of surface pressure variability in the modern climate. We find a strong
38 correlation ($r = -0.94$, $p < 0.01$) between site-average $^{86}\text{Kr}_{\text{xs}}$ and site synoptic variability from reanalysis
39 data. The main uncertainties in the method are the corrections for gas loss and thermal fractionation, and
40 the relatively large scatter in the data. We show $^{86}\text{Kr}_{\text{xs}}$ is linked to the position of the eddy-driven subpolar
41 jet (SPJ), with a southern position enhancing pressure variability.

42 We present a $^{86}\text{Kr}_{\text{xs}}$ record covering the last 24 ka from the WAIS Divide ice core. West Antarctic synoptic
43 activity is slightly below modern levels during the last glacial maximum (LGM); increases during the
44 Heinrich Stadial 1 and Younger Dryas North Atlantic cold periods; weakens abruptly at the Holocene onset;
45 remains low during the early and mid-Holocene, and gradually increases to its modern value. The WAIS
46 Divide $^{86}\text{Kr}_{\text{xs}}$ record resembles records of monsoon intensity thought to reflect changes in the meridional
47 position of the intertropical convergence zone (ITCZ) on orbital and millennial timescales, such that West
48 Antarctic storminess is weaker when the ITCZ is displaced northward, and stronger when it is displaced
49 southward. We interpret variations in synoptic activity as reflecting movement of the South Pacific SPJ in
50 parallel to the ITCZ migrations, which is the expected zonal-mean response of the eddy-driven jet in models
51 and proxy data. Past changes to Pacific climate and the El Niño Southern Oscillation (ENSO) may amplify
52 the signal of the SPJ migration. Our interpretation is broadly consistent with opal flux records from the
53 Pacific Antarctic zone thought to reflect wind-driven upwelling.

54 We emphasize that $^{86}\text{Kr}_{\text{xs}}$ is a new proxy, and more work is called for to confirm, replicate and better
55 understand these results; until such time, our conclusions regarding past atmospheric dynamics remain
56 tentative. Current scientific understanding of firn air transport and trapping is insufficient to explain all the
57 observed variations in $^{86}\text{Kr}_{\text{xs}}$.



58 **1 Introduction**

59 **1.1 Motivation and objectives**

60 Proxy records from around the globe show strong evidence for past changes in Earth's atmospheric
61 circulation and hydrological cycle that often far exceed those seen in the relatively short instrumental
62 period.

63 For example, low-latitude records of riverine discharge captured in ocean sediments (Peterson et al., 2000),
64 and isotopic composition of meteoric water captured in dripstone calcite (Cheng et al., 2016), suggest large
65 variations in tropical hydrology and monsoon strength, commonly interpreted as meridional migrations of
66 the intertropical convergence zone or ITCZ (Chiang and Friedman, 2012; Schneider et al., 2014). Such
67 ITCZ movement is seen both in response to insolation changes linked to planetary orbit (Cruz et al., 2005)
68 as well as in response to the abrupt millennial-scale Dansgaard-Oeschger (D-O) and Heinrich cycles of the
69 North-Atlantic (Kanner et al., 2012; Wang et al., 2001); the organizing principle is that the ITCZ follows
70 the thermal equator and therefore migrates towards the warmer (or warming) hemisphere (Broccoli et al.,
71 2006; Chiang and Bitz, 2005).

72 As a second example, the intensity of the El Niño – Southern Oscillation (ENSO), the dominant mode of
73 global interannual climate variability, has changed through time. A variety of proxy data suggest ENSO
74 activity in the 20th century was much stronger than in preceding centuries (Emile-Geay et al., 2015; Fowler
75 et al., 2012; Gergis and Fowler, 2009; Thompson et al., 2013). The vast majority of data and model studies
76 suggest weakened ENSO strength in the mid- and early-Holocene, likely in response to stronger orbitally-
77 driven NH summer insolation at that time (Braconnot et al., 2012; Cane, 2005; Clement et al., 2000; Driscoll
78 et al., 2014; Koutavas et al., 2006; Liu et al., 2000; Liu et al., 2014; Moy et al., 2002; Rein et al., 2005;
79 Tudhope et al., 2001; Zheng et al., 2008); yet other studies suggest there may not be such a clear trend, and
80 simply more variability (Cobb et al., 2013). Intensification of ENSO (or perhaps a more El-Niño-like mean
81 state) may have occurred during the North-Atlantic cold phases of the abrupt D-O and Heinrich cycles
82 (Braconnot et al., 2012; Merkel et al., 2010; Stott et al., 2002; Timmermann et al., 2007). Overall,
83 understanding past and future ENSO variability remains extremely challenging (Cai et al., 2015).

84 As a last example, the strength and meridional position of the southern hemisphere westerlies (SHW) is
85 thought to have changed in the past, which, via Southern Ocean wind-driven upwelling, has potential
86 implications for the global overturning circulation (Marshall and Speer, 2012) and for carbon storage in the
87 abyssal ocean (Anderson et al., 2009; Russell et al., 2006; Toggweiler et al., 2006). The SHW are thought
88 to be shifted equatorward (Kohfeld et al., 2013) during the last glacial maximum (LGM), a shift on which
89 climate models disagree (Rojas et al., 2009; Sime et al., 2013). During the abrupt D-O and Heinrich cycles,
90 the SHW move in parallel with the aforementioned migrations of the ITCZ in both data (Buizert et al.,
91 2018; Marino et al., 2013; Markle et al., 2017) and models (Lee et al., 2011; Pedro et al., 2018; Rind et al.,
92 2001).

93 As these examples clearly illustrate, evidence of past changes to the large-scale atmospheric circulation is
94 widespread. However, proxy evidence of such past changes is typically indirect – for example via isotopes
95 in precipitation, sea surface temperature, ocean frontal positions, windblown dust, or ocean upwelling –
96 complicating their interpretation. Here we present a newly developed noble gas-based ice core proxy, Kr-



97 $^{86}\text{Kr}_{\text{xs}}$), that directly samples a component of the large-scale atmospheric circulation: synoptic-
98 scale pressure variability. Owing to the firm air residence time of several years (Buizert et al., 2013) and the
99 gradual bubble trapping process, each ice core sample contains a distribution of gas ages, rather than a
100 single age. Therefore, $^{86}\text{Kr}_{\text{xs}}$ does not record the passing of individual weather systems, but rather the time-
101 average intensity of synoptic-scale barometric variability.

102 Here we provide the first complete description of this new proxy. We validate and calibrate $^{86}\text{Kr}_{\text{xs}}$ using
103 late-Holocene ice core samples from locations around Antarctica and Greenland that represent a wide range
104 of pressure variability in the modern climate. We discuss the difficulties in using this proxy (analytical
105 precision, surface melt, corrections for sample gas loss and thermal fractionation). Next, we use reanalysis
106 data to better understand the drivers of surface pressure variability in Antarctica. Last, we present an $^{86}\text{Kr}_{\text{xs}}$
107 records from the Antarctic WAIS Divide ice core through the last deglaciation.

108 1.2 Gravitational disequilibrium and Kr-86 excess

109 The upper 50-100 m of the ice sheet accumulation zone consists of firm, the unconsolidated intermediate
110 stage between snow and ice. An interconnected pore network exists within the firm, in which gas transport
111 is dominated by molecular diffusion (Schwander et al., 1993). Diffusion in this stagnant air column results
112 in gravitational enrichment in heavy gas isotopic ratios such as $\delta^{15/14}\text{N-N}_2$, $\delta^{40/36}\text{Ar}$ and $\delta^{86/82}\text{Kr}$ (Schwander,
113 1989; Sowers et al., 1992). In gravitational equilibrium, all these gases attain the same degree of isotopic
114 enrichment per unit mass difference:

$$115 \quad \delta_{\text{grav}}(z) = \left[\exp\left(\frac{\Delta m g z}{RT}\right) - 1 \right] \times 1000\text{‰} \quad (1)$$

116 with Δm the isotopic mass difference ($1 \times 10^{-3} \text{ kg mol}^{-1}$), g the gravitational acceleration, z the depth, R the
117 gas constant and T the Kelvin temperature.

118 Besides molecular diffusion, firm air is mixed and transported via three other processes: downward
119 advection with the sinking ice matrix, convective mixing (used in the firm air literature as an umbrella term
120 to denote vigorous air exchange with the atmosphere via e.g. wind pumping and seasonal convection), and
121 dispersive mixing. These last three transport processes are all driven by large-scale air movement that does
122 not distinguish between isotopologues, and we refer to them collectively as macroscopic air movement. Of
123 particular interest for our proxy is dispersive mixing, which is driven by surface pressure variations. When
124 a low-pressure (high-pressure) system moves into the site, firm air at all depth levels is forced upwards
125 (downwards) to reach hydrostatic equilibrium with the atmosphere – a process called barometric pumping.
126 One can think of the firm layer “breathing” in and out in response to a rising and falling barometer,
127 respectively. Because firm has a finite dispersivity (Schwander et al., 1988), this air movement mixes the
128 interstitial firm air (Buizert and Severinghaus, 2016).

129 Any type of macroscopic air movement disturbs the gravitational settling, reducing isotopic enrichment
130 below δ_{grav} . Let $\delta^{86}\text{Kr}$, $\delta^{40}\text{Ar}$, and $\delta^{15}\text{N}$ refer to deviations of $^{86}\text{Kr}/^{82}\text{Kr}$, $^{40}\text{Ar}/^{36}\text{Ar}$, and $^{29}\text{N}_2/^{28}\text{N}_2$, respectively,
131 from their ratios in the well-mixed atmosphere. Gases that diffuse faster (such as N_2) will always be closer
132 to gravitational equilibrium than gases that diffuse slower (such as Kr), and in the absence of thermal
133 fractionation $\delta^{86}\text{Kr}/4 < \delta^{40}\text{Ar}/4 < \delta^{15}\text{N} < \delta_{\text{grav}}$. The isotopic differences $\delta^{86}\text{Kr}/4 - \delta^{40}\text{Ar}/4$ and $\delta^{86}\text{Kr}/4 - \delta^{15}\text{N}$
134 thus reflect the degree of gravitational disequilibrium. The magnitudes of the isotopic disequilibria scale in



135 a predictable way following the molecular diffusion coefficients (Birner et al., 2018); because the diffusion
136 coefficients of N₂ and Ar are very similar, their disequilibria are comparable in magnitude. We define Kr-
137 86 excess using the Kr and Ar isotopic difference:

$$138 \quad {}^{86}\text{Kr}_{\text{xs}40} = \frac{\delta^{86}\text{Kr}_{\text{corr}} - \delta^{40}\text{Ar}_{\text{corr}}}{\delta^{40}\text{Ar}_{\text{corr}}} \times 1000 \text{ per meg } \text{‰}^{-1} \quad (2)$$

139 where the “corr” subscript denotes a correction for gas loss (Appendix A1) and thermal fractionation
140 (Appendix A2). The rationale for including a normalization in the denominator is discussed below. An
141 alternative Kr-86 excess definition is possible using $\delta^{15}\text{N}$ instead of $\delta^{40}\text{Ar}$:

$$142 \quad {}^{86}\text{Kr}_{\text{xs}15} = \frac{\delta^{86}\text{Kr}_{\text{corr}}/4 - \delta^{15}\text{N}_{\text{corr}}}{\delta^{15}\text{N}_{\text{corr}}} \times 1000 \text{ per meg } \text{‰}^{-1} \quad (3)$$

143 The ${}^{86}\text{Kr}_{\text{xs}40}$ definition is preferred, because it is less sensitive to thermal fractionation making it more
144 suitable for interpreting time series. Unless explicitly stated otherwise, we use ${}^{86}\text{Kr}_{\text{xs}40}$ as our definition of
145 Kr-86 excess. The ${}^{86}\text{Kr}_{\text{xs}15}$ does provide a way to check the validity of ${}^{86}\text{Kr}_{\text{xs}40}$ timeseries, and indeed we
146 find good correspondence between both definitions for the WDC deglacial timeseries (Fig. 6). Because the
147 disequilibrium signal is small, we express ${}^{86}\text{Kr}_{\text{xs}}$ in units of per meg (parts per million) of gravitational
148 disequilibrium per ‰ of gravitational enrichment.

149 In the (theoretical) case of full gravitational equilibrium (and no gas loss or thermal fractionation), $\delta^{86}\text{Kr}/4$
150 $= \delta^{40}\text{Ar}/4 = \delta^{15}\text{N} = \delta_{\text{grav}}$, and therefore ${}^{86}\text{Kr}_{\text{xs}} = 0$. Any type of macroscopic mixing will cause $\delta^{86}\text{Kr}/4 <$
151 $\delta^{40}\text{Ar}/4 < \delta^{15}\text{N} < \delta_{\text{grav}}$, and thus ${}^{86}\text{Kr}_{\text{xs}} < 0$. In this sense ${}^{86}\text{Kr}_{\text{xs}}$ is a quantitative measure for the degree of
152 gravitational disequilibrium in the firm layer (Birner et al., 2018; Buizert and Severinghaus, 2016).

153 Kawamura et al. (2013) first describe this gravitational disequilibrium (or kinetic) fractionation effect at
154 the Megadunes site (Severinghaus et al., 2010), where deep firm cracking leads to a 23 m-thick convective
155 zone. They suggest that the isotopic disequilibrium can be used to estimate past convective zone thickness.
156 We show here that sites with small convective zones can nevertheless have very negative ${}^{86}\text{Kr}_{\text{xs}}$, and instead
157 we suggest that the ice core ${}^{86}\text{Kr}_{\text{xs}}$ is dominated by dispersive mixing driven by barometric pumping from
158 synoptic-scale pressure variability.

159 The principle behind ${}^{86}\text{Kr}_{\text{xs}}$ is illustrated with idealized firm model experiments in Fig. 1. In the absence of
160 dispersive mixing (Fig. 1A, left panel), all isotope ratios approach δ_{grav} and $\delta^{86}\text{Kr} - \delta^{40}\text{Ar}$ is close to zero –
161 but not exactly zero owing to downward air advection. Next, we replace a fraction f of the molecular
162 diffusion with dispersive mixing. With dispersive mixing at $f = 0.1$ and $f = 0.2$ of total mixing (middle and
163 right panels, respectively), isotopic enrichment is progressively reduced below δ_{grav} (dashed line), making
164 $\delta^{86}\text{Kr} - \delta^{40}\text{Ar}$ (and consequently ${}^{86}\text{Kr}_{\text{xs}}$) increasingly negative.

165 The ratio of macroscopic over diffusive transport is expressed via the dimensionless Péclet number, given
166 here for advection and dispersion:

$$167 \quad \text{Pe}_X = \frac{w_{\text{air}}L + D_{\text{disp}}}{D_X} \quad (4)$$



168 where \mathbf{Pe}_X is the Péclet number for gas X , w_{air} the (downward) advective air velocity, L a characteristic
169 length scale, D_X the diffusion coefficient for gas X , and D_{disp} is the dispersion coefficient (Buizert and
170 Severinghaus, 2016). In agreement with earlier studies (Birner et al., 2018; Kawamura et al., 2013), we find
171 that $\delta^{86}\text{Kr} - \delta^{40}\text{Ar}$ is maximized when molecular and dispersive mixing are equal in magnitude ($f=0.5$, Fig.
172 1B), corresponding to $\mathbf{Pe}_X \approx 1$. Note that $^{86}\text{Kr}_{\text{xs}}$ responds more linearly to f than $\delta^{86}\text{Kr} - \delta^{40}\text{Ar}$ does, due to
173 $\delta^{40}\text{Ar}$ in the denominator of Eq. (2).

174 In a last idealized experiment, we keep the fraction of dispersion fixed at $f=0.1$ while we reduce the
175 thickness of the firn column by increasing the site temperature (Fig. 1C). We find that $\delta^{86}\text{Kr} - \delta^{40}\text{Ar}$ scales
176 linearly with firn thickness, here represented by $\delta^{40}\text{Ar}$ on the x-axis. However, $^{86}\text{Kr}_{\text{xs}}$ remains essentially
177 constant due to the normalization by $\delta^{40}\text{Ar}$ in the denominator of Eq. (2). The normalization step is thus
178 necessary to enable meaningful comparison between different sites and time periods that all have different
179 firn thicknesses. For this reason, the definition of $^{86}\text{Kr}_{\text{xs}}$ used here has been updated from the original
180 definition by (Buizert and Severinghaus, 2016).

181 Note that these highly idealized experiments assume dispersive mixing to be a fixed fraction of total
182 transport throughout the firn column, equivalent to a constant Péclet number in the diffusive zone (a
183 convective zone is absent in these simulations). In reality, the Péclet number varies greatly on all spatial
184 scales. On the macroscopic scale (> 1 m), Pe reflects the various transport regimes (Sowers et al., 1992),
185 being highest in the convective and lock-in zones. On the microscopic scale (< 1 cm), hydraulic
186 conductance scales as $\propto r^4$ (with r the pore radius) whereas the diffusive conductance scales as $\propto r^2$. This
187 means that the Darcy flow associated with barometric pumping will concentrate in the widest pores and
188 pathways, leading to a range of effective Péclet numbers within a single sample of firn. At intermediate
189 spatial scales of a few cm, firn density layering introduces strong heterogeneity in transport properties. It is
190 unclear at present whether the competition between diffusive and non-diffusive transport, which occurs at
191 the microscopic pore level, can be accurately represented in macroscopic firn air models via a linear
192 parameterization as is the current practice.

193



194 2 Methods

195 2.1 Ice core sites

196 In this study we use ice samples from eleven ice cores drilled in Antarctica, and one in Greenland. The
197 Antarctic sites are: West Antarctic Ice Sheet (WAIS) Divide core (WDC06A, or WDC), Siple Dome
198 (SDM), James Ross Island (JRI), Bruce Plateau (BP), Law Dome DE08, Law Dome DE08-OH, Law Dome
199 DSSW20K, Roosevelt Island Climate Evolution (RICE), Dome Fuji (DF), EPICA (European Project for
200 Ice Coring in Antarctica) Dome C (EDC), and South Pole Ice Core (SPC14, or SP). Ice core locations in
201 Antarctica are shown in Fig. 2A. In Greenland, we use samples from the Greenland Ice Sheet Project 2
202 (GISP2).

203 We shall refer to late Holocene data from these sites as the calibration dataset, analogous to a core top data
204 set in the sediment coring literature. Site characteristics, coordinates, and number of samples included in
205 the calibration data set are given in Table 1. The DE08-OH site is a recent revisit of the Law Dome DE08
206 site. The DE08-OH core was measured at sub-annual resolution to understand cm-scale $^{86}\text{Kr}_{\text{xs}}$ variations
207 due to for example layering in firn density and bubble trapping (Appendix B). In addition to the calibration
208 data set, we present a record of Kr-86 excess going back to the LGM from WDC.

209 2.2 Ice sample analysis

210 We broadly follow analytical procedures described elsewhere (Bereiter et al., 2018a; Bereiter et al., 2018b;
211 Headly and Severinghaus, 2007; Severinghaus et al., 2003). In short, an 800 g ice sample, its edges trimmed
212 with a band saw to expose fresh surfaces, is placed in a chilled vacuum flask that is then evacuated for 20
213 minutes using a turbomolecular pump. Air is extracted from the ice by melting the sample while stirring
214 vigorously with a magnetic stir bar, led through a water trap, and cryogenically trapped in a dip tube
215 immersed in liquid He. Next, the sample is split into two unequal fractions. The smaller fraction (about 2%
216 of total air) is analyzed for $\delta^{15}\text{N-N}_2$, $\delta^{18}\text{O-O}_2$, $\delta\text{O}_2/\text{N}_2$ and $\delta\text{Ar}/\text{N}_2$ on a 3kV Thermo Finnigan Delta V plus
217 dual inlet IRMS (isotope ratio mass spectrometer). In the larger fraction, noble gases are isolated via hot
218 gettering to remove reactive gases. The purified noble gases are then analyzed for $\delta^{40/36}\text{Ar}$, $\delta^{40/38}\text{Ar}$, $\delta^{86/82}\text{Kr}$,
219 $\delta^{86/84}\text{Kr}$, $\delta^{86/83}\text{Kr}$, $\delta\text{Kr}/\text{Ar}$ and $\delta\text{Xe}/\text{Ar}$ on a 10kV Thermo Finnigan MAT253 dual inlet IRMS. We reject
220 one sample from RICE due to incomplete sample transfer, and one sample from WDC due to problems
221 with the water trap. Calibration is done for each measurement campaign by running samples of La Jolla
222 pier air.

223 All calibration (core top) data were measured using “Method 2” as described by Bereiter et al. (2018a),
224 with a longer equilibration time during the splitting step than used in that study to improve isotopic
225 equilibration between the fractions. The exception is the DE08-OH site, where the ice sample (rather than
226 the extracted gas sample) was split into two fractions – the advantage of this approach is that it does not
227 require a gas splitting step that is time-consuming and may fractionate the isotopes; the downside is that
228 the samples may have slightly different isotopic composition due to the stochastic nature of bubble trapping
229 and the different gas-loss histories of the ice pieces.

230 Measurements of the WDC downcore data set were performed over five separate measurement campaigns
231 that occurred in February-April 2014, February-April 2015, August 2015, August 2020, and August 2021,



232 respectively. The first three campaigns are described by Bereiter et al. (2018b), in which the $^{86}\text{Kr}_{\text{xs}}$ data are
233 a by-product of measuring $\delta\text{Kr}/\text{N}_2$ for reconstructing global mean ocean temperature. Campaigns 1 and 2
234 are in good agreement, whereas campaign 3 appears offset from the other two by an amount that exceeds
235 the analytical precision (offset around 35 per meg ‰^{-1}). To validate the main features in the record, we
236 performed two additional campaigns (4 and 5), in which all the gas extracted from each ice sample was
237 quantitatively gettered and only analysed for Ar and Kr isotopic composition. The downcore record, as well
238 as the five analytical campaigns, are discussed in detail in section 5.1. Data from the bubble-clathrate
239 transition zone (here 1000 to 1500 m depth, or ~4ka to 7ka BP are excluded owing to the potential for
240 artefacts.

241 All samples were analyzed at Scripps Institution of Oceanography, USA, with the exception of the EDC
242 samples which were analyzed at University of Bern, Switzerland (Baggenstos et al., 2019). Some of the
243 EDC samples analyzed had clear evidence of drill liquid contamination, which acts to artefactually lower
244 $^{86}\text{Kr}_{\text{xs}}$; the late Holocene data used here were not flagged for drill liquid contamination.

245 The 2σ analytical precision of the $\delta^{15}\text{N}$, $\delta^{40}\text{Ar}$, and $\delta^{86}\text{Kr}$ measurements is around 3, 5 and 26 per meg,
246 respectively, based on the reproducibility of La Jolla Air measurements. Via standard error propagation,
247 this results in a ~ 22 per meg ‰^{-1} (2σ) analytical uncertainty for both $^{86}\text{Kr}_{\text{xs}40}$ and $^{86}\text{Kr}_{\text{xs}15}$. We have no true
248 (same-depth) replicates to assess the reproducibility of $^{86}\text{Kr}_{\text{xs}}$ measurements experimentally. The measured
249 isotope ratios are corrected for gas loss (Δ_{GL}^{40}) and thermal fractionation (Δ_{TF}^{86} , Δ_{TF}^{40} , Δ_{TF}^{15}) before
250 interpretation; details on these corrections are given in appendix A. For the coretop calibration study, the
251 average magnitude of the gas loss and thermal fractionation corrections is +14 and -15 per meg ‰^{-1} in
252 $^{86}\text{Kr}_{\text{xs}}$, respectively.

253 Our study includes two ice cores from the Antarctic Peninsula: BP (2 ice samples) and JRI (5 ice samples).
254 Measured $\delta\text{Xe}/\text{N}_2$ ratios (and to a lesser extent the $\delta\text{Kr}/\text{N}_2$ ratios) in all samples from both locations are
255 significantly elevated above the expected gravitational enrichment signal (Fig. A1A), which is clear
256 evidence for the presence of refrozen meltwater in these samples (Orsi et al., 2015). Like xenon, krypton is
257 highly soluble in (melt)water, and therefore $^{86}\text{Kr}_{\text{xs}}$ cannot be reliably measured in these samples; we reject
258 all samples from the BP and JRI sites. It is notable that all samples from both sites show evidence of refrozen
259 meltwater, given that the high-accumulation BP core is nearly entirely free of visible melt layers, and that
260 we carefully selected samples without visible melt features at JRI. Visible ice lenses form only when
261 meltwater pools and refreezes on top of low-permeability layers such as wind crusts; our observations
262 suggest meltwater can also refreeze throughout the firn in a way that cannot be detected visually.

263



264 3 Calibrating Kr-86 excess

265 The $^{86}\text{Kr}_{\text{xs}}$ proxy for synoptic activity was first proposed on theoretical grounds by Buizert and
266 Severinghaus (2016) – here we provide the first experimental validation of this proxy using a coretop
267 calibration of $^{86}\text{Kr}_{\text{xs}}$ using late-Holocene ice core samples from nine locations around Antarctica and one in
268 Greenland that represent a wide range of pressure variability in the modern climate.

269 3.1 Spatial variation in synoptic-scale pressure variability

270 Kr-86 excess is sensitive to air movement (both upward and downward), which in turn is controlled by the
271 magnitude of relative air pressure change. Let p_i be a time series of (synoptic-scale) site surface pressure
272 with N data points, time resolution Δt , and mean value \bar{p} . The time series can span a month, year, or multi-
273 year period, with \bar{p} potentially different for each month or year. We define the parameter Φ as:

$$274 \quad \Phi = \frac{1}{N\bar{p}} \sum_{i=1}^N \left| \frac{p_i - p_{i-1}}{\Delta t} \right| \quad (5)$$

275 which we here express in convenient units of $\% \text{ day}^{-1}$. Φ reflects the intensity of barometric pumping in the
276 firn column. Note that Δt should be larger than ~ 1 hour (the timescale for the entire firn column to
277 equilibrate with the surface pressure), and smaller than about a day (in order to adequately resolve synoptic-
278 scale pressure events). Here we use ERA-interim reanalysis data from 1979-2017 with $\Delta t = 6$ hours (Dee
279 et al., 2011), from which we calculate monthly and annual Φ values using Eq. (5). A map of annual-mean
280 Φ across Antarctica is given in Fig. 2A. At all sites considered, Φ has a strong seasonal cycle with pressure
281 variability/storminess being strongest in the local winter season (Fig. 2C). Interannual variability in Φ is
282 greatest along the Siple coast and coastal West Antarctica (Fig. 2B), mainly reflecting the influence of
283 central Pacific (ENSO, PDO) climate variability (Section 4).

284 3.2 Kr-86 excess proxy calibration

285 Present-day Antarctica has a wide range of Φ (Fig. 2A), which allows us to validate and calibrate $^{86}\text{Kr}_{\text{xs}}$. In
286 Fig. 3A we plot the site mean $^{86}\text{Kr}_{\text{xs}40}$ (with $\pm 1\sigma$ error bars) as a function of Φ . We find a Pearson correlation
287 coefficient of $r = -0.94$ when using site mean $^{86}\text{Kr}_{\text{xs}40}$, and $r = -0.83$ when using the $^{86}\text{Kr}_{\text{xs}40}$ of individual
288 samples, respectively ($p < 0.01$). Note that in this particular case the site-mean $^{86}\text{Kr}_{\text{xs}40}$ and $^{86}\text{Kr}_{\text{xs}15}$ are
289 identical (because by design, after thermal correction $\delta^{15}\text{N} = \delta^{40}\text{Ar}$); the error bars are different, though.

290 The $^{86}\text{Kr}_{\text{xs}}$ data have been corrected for gas loss (Appendix A1) and thermal fractionation (Appendix A2);
291 with the gas loss correction being the more uncertain component. Figure 3B shows the correlations of the
292 calibration curve as a function of the gas loss scaling parameter ϵ_{40} . We find a good correlation over a wide
293 range of ϵ_{40} values, proving our calibration is not dependent on the choice of ϵ_{40} . When using uncorrected
294 $^{86}\text{Kr}_{\text{xs}40}$ data the site mean correlation is $r = -0.71$; when applied individually, both the gas loss and thermal
295 correction each improve the correlation to $r = -0.77$ and $r = -0.79$, respectively (Fig. A3, all $p < 0.05$). Based
296 on these tests we conclude that the observed relationship is not an artefact of the applied corrections. The
297 applied corrections improve the correlation, which increases confidence in the method. The calibration
298 results for $^{86}\text{Kr}_{\text{xs}15}$ are shown in Fig. A4.



299 Notably, there is a large spread in $^{86}\text{Kr}_{\text{xs}}$ across samples from a single site, particularly at the high Φ sites
300 of SDM and RICE (note the $\pm 1\sigma$ error bars). This spread is larger than the measurement uncertainty, and
301 we believe this variance reflects a signal that is truly present in the ice. The Siple coast and Roosevelt Island
302 experience the largest Φ interannual variability in Antarctica (Fig. 2B), and it is therefore likely that our
303 coarse sampling is aliasing the true $^{86}\text{Kr}_{\text{xs}}$ signal. The variance in $^{86}\text{Kr}_{\text{xs}}$ may contain climate information
304 also; this is reminiscent of the way in which the variance (rather than the mean) of $\delta^{18}\text{O}$ in individual
305 planktic foraminifera in ocean sediment samples from the equatorial Pacific can be used as a proxy for
306 past ENSO variability (Koutavas et al., 2006).

307 Both theoretical considerations and observations thus suggest $^{86}\text{Kr}_{\text{xs}}$ is a proxy for barometric surface
308 pressure variability at the site, and in the remainder of this manuscript we will interpret it as such.

309 **3.3 Discussion of the Kr-86 excess proxy**

310 Our interpretation of $^{86}\text{Kr}_{\text{xs}}$ as a proxy for pressure variability is somewhat complicated by the possibility
311 of deep convective zones, which have the same $^{86}\text{Kr}_{\text{xs}}$ signature as barometric pumping. This was
312 discovered at the Megadunes (MD) site, central East Antarctica; at this zero-accumulation site deep cracks
313 form in the firn layer that facilitate a 23 m deep convection zone (Severinghaus et al., 2010). In fact, this
314 observation led earlier work to suggest that noble gas gravitational disequilibrium may be used as a proxy
315 for convective zone thickness (Kawamura et al., 2013), rather than synoptic-scale pressure variability as
316 suggested here. Although megadunes and zero-accumulation zones are ubiquitous and cover 20% of the
317 Antarctic Plateau (Fahnestock et al., 2000), ice cores are seldom drilled in these areas and it is safe to
318 assume that they never formed at sites like WAIS Divide that had relatively high accumulation rates even
319 during the last glacial period. Performing the corrections for thermal and size-dependent fractionation is
320 challenging at MD, and we suggest that the MD $^{86}\text{Kr}_{\text{xs}}$ is in the range of -2 to -55 per meg ‰^{-1} ; even at the
321 larger limit, this is still smaller in magnitude than $^{86}\text{Kr}_{\text{xs}}$ anomalies at several modern-day sites with small
322 convective zones (such as SDM, RICE and the Law Dome sites), suggesting barometric pumping is capable
323 of producing larger $^{86}\text{Kr}_{\text{xs}}$ signals than even the most extreme observed case of convective surface mixing.
324 Having $^{86}\text{Kr}_{\text{xs}}$ measured in MD ice core (rather than firn air) samples would be valuable for a more
325 meaningful comparison to the ice core sample measurements presented here. Windy sites can have
326 substantial convective zones of ~ 14 m (Kawamura et al., 2006), and future studies of $^{86}\text{Kr}_{\text{xs}}$ at such sites
327 would be valuable.

328 Currently, 1-D and 2-D firn air transport model simulations underestimate the magnitude of the $^{86}\text{Kr}_{\text{xs}}$ signal
329 compared to measurements in mature ice samples (Birner et al., 2018), complicating scientific
330 understanding of the proxy. In these models, the effective molecular diffusivity of each gas is scaled linearly
331 to its free air diffusivity. The ratio of krypton to argon free air diffusivity is 0.78. This ratio, which directly
332 sets the magnitude of the simulated $^{86}\text{Kr}_{\text{xs}}$, may actually be smaller than 0.78 in real firn, as krypton is more
333 readily adsorbed onto firn surfaces retarding its movement (similar to gasses moving through a gas
334 chromatography column). This may be one explanation for why models simulate too little $^{86}\text{Kr}_{\text{xs}}$.

335 Another likely explanation for the model-data mismatch is that certain critical sub-grid processes (such as
336 the aforementioned pore-size dependence of the Péclet number) are not adequately represented in these
337 models. Barometric pumping may further actively shape the pore network through the movement of water
338 vapor, thereby keeping certain preferred pathways connected and open below the density where percolation



339 theory would predict their closure (Schaller et al., 2017). The fate of a pore restriction is determined by the
340 balance between the hydrostatic pressure (that acts to close it) and vapor movement away from its convex
341 surfaces (that acts to keep it open); we speculate that barometric Darcy air flow keeps high-flow channels
342 connected longer by eroding convex surfaces. This enhances the complexity (and therefore dispersivity) of
343 the deep firn pore network and possibly creates a non-linear $^{86}\text{Kr}_{\text{xs}}$ response to barometric pumping. The
344 hypothesized channel formation in deep firn is driven by a positive feedback on flow volume, and somewhat
345 reminiscent of erosion-driven stream network formation in fluvial geomorphology.

346 Firn models predict that the gravitational disequilibrium effect in elemental ratios (such as $\delta\text{Kr}/\text{Ar}$) should
347 be proportional to that in isotopic ratios. However, the observations suggest that the former is usually
348 smaller than would be expected from the latter. We do not have an explanation for this effect. Including
349 measurements of xenon isotopes and elemental ratios in future measurement campaigns may be able to
350 provide additional constraints to better understand this discrepancy.

351 Measurements on firn air samples, where available, suggest a smaller $^{86}\text{Kr}_{\text{xs}}$ anomaly in firn air than found
352 in ice core samples from the same site. We attribute this in part to a seasonal bias that is introduced by the
353 fact that firn air sampling always takes place during the summer months, whereas the synoptic variability
354 that drives the Kr-86 excess anomalies is largest during the winter (Fig. 2C); consequently, firn air
355 observations are biased towards weaker $^{86}\text{Kr}_{\text{xs}}$. Further, in the deep firn where $^{86}\text{Kr}_{\text{xs}}$ anomalies are largest,
356 firn air pumping may not yield a representative air sample, but rather be biased towards the well-connected
357 porosity at the expense of poorly-connected cul-de-sac-like pore clusters. Since barometric pumping
358 ventilates this well-connected porespace with low- $^{86}\text{Kr}_{\text{xs}}$ air from shallower depths, the firn air sampling
359 may not capture a representative $^{86}\text{Kr}_{\text{xs}}$ value of the full firn air content. These explanations are all somewhat
360 speculative, and a definitive understanding of the firn-ice differences is lacking at this stage.

361 Gas loss and thermal corrections are critical to the interpretation of $^{86}\text{Kr}_{\text{xs}}$. The thermal correction is applied
362 to account for thermal gradients in the firn (ΔT , here defined as the temperature at the top minus the
363 temperature at the base of the firn), which are chiefly caused by geothermal heat or surface temperature
364 changes at the site. At low-accumulation sites geothermal heating leads to $\Delta T < 0$. We use ^{15}N -excess ($\delta^{15}\text{N}$
365 $- \delta^{40}\text{Ar}/4$) to estimate the thermal gradient in the firn (Appendix A2). Because nitrogen and argon have
366 similar diffusivities but different thermal diffusion coefficients, $\delta^{15}\text{N} - \delta^{40}\text{Ar}$ is relatively insensitive to
367 barometric pumping yet sensitive to thermal fractionation, allowing estimating ΔT .

368 Besides the actual thermal gradients in the firn, the isotopic composition may also be impacted by seasonal
369 rectifier effects. If the firn air transport properties differ between the seasons (for example due to thermal
370 contraction cracks, convective instabilities, or seasonality in wind pumping), this can result in a thermal
371 fractionation of isotopic ratios in the absence of a thermal gradient (Morgan et al., 2022).

372 For the WDC, DSS and GISP2 sites we obtain ΔT values close to zero as expected for these high-
373 accumulation sites; for the SP, SDM, RICE, and DF sites we find ΔT ranging from -0.76 to -1.18°C , in
374 agreement with the effect of geothermal heat. The high-accumulation DE08 and DE08-OH sites both have
375 an unexpectedly large ΔT of -1.6°C ; the good agreement between the sites suggest it is likely a real signal,
376 yet we can rule out geothermal heat as the cause. This may suggest that the Law Dome DE08 site is subject
377 to a seasonal rectifier effect, or a recent climatic cooling. Last, the EDC site shows an unexpected $\Delta T =$



378 $+1.6 \pm 1.89^\circ\text{C}$. Three possible explanations are: (1) the aforementioned drill liquid contamination for this
379 core; (2) a summertime-biased seasonal rectifier; or (3) an over-correction of $\delta^{40}\text{Ar}$ for gas loss, which
380 could occur for example if natural and post-coring fugitive gas loss fractionate $\delta^{40}\text{Ar}$ differently and EDC
381 samples were impacted mostly by the former type (our correction is mostly based on measurements of the
382 latter type).

383 For the Law Dome DE08-OH site we observe large (5-fold) sub-annual variations in $^{86}\text{Kr}_{\text{xs}}$ (Fig. B1). The
384 magnitude of the $^{86}\text{Kr}_{\text{xs}}$ layering is truly remarkable. The isotopic enrichment of each gas ($\delta^{15}\text{N}$, $\delta^{40}\text{Ar}$,
385 $\delta^{86}\text{Kr}$) can be converted to an effective diffusive column height (DCH). For the samples with the smallest
386 (greatest) $^{86}\text{Kr}_{\text{xs}}$ magnitude, this DCH is around 1 m (6 m) shorter for $\delta^{86}\text{Kr}$ than it is for $\delta^{15}\text{N}$. The firm air
387 transport physics that may explain such phenomena are beyond our current scientific understanding. The
388 sub-annual variations may be related to the seasonal cycle in storminess (Fig. 2C), though that seems
389 improbable as the gas age distribution at the depth of bubble closure has a width of several years (Schwander
390 et al., 1993). Another reason may be seasonal layering in firm properties – such as density, grain size, and
391 pore connectivity – that control the degree of disorder and dispersive mixing occurring in the firm, and lead
392 to a staggered firm trapping and seasonal variations in Δage (Etheridge et al., 1992; Rhodes et al., 2016).
393 The sample air content estimated from the IRMS inlet pressure is similar for all measurements, making it
394 unlikely that the variations in $^{86}\text{Kr}_{\text{xs}}$ are caused by remnant open porosity in lower-density layers. In any
395 case it is remarkable that such large variations in gas composition can arise and persist on such small length
396 scales, given the relatively large diffusive, dispersive, and advective transport length scales of the system.
397 More work is needed to establish the origin of the sub-annual variations in ice core $^{86}\text{Kr}_{\text{xs}}$.

398 Another puzzling observation is the positive $^{86}\text{Kr}_{\text{xs}}$ at the Dome Fuji (DF) site; theoretical considerations
399 suggest it should always be negative. In part this may be due to an over-correction of $\delta^{40}\text{Ar}$ for gas loss,
400 which would act to bias $^{86}\text{Kr}_{\text{xs}}$ in the positive direction. This correction is largest at DF owing to the very
401 negative $\delta\text{O}_2/\text{N}_2$ and $\delta\text{Ar}/\text{N}_2$ (Fig. A1); while we base our correction on published work, it is conceivable
402 that we overestimate the true correction (Appendix A1). In particular, our gas loss correction is based on
403 observations on artefactual post-coring gas loss, which may fractionate $\delta^{40}\text{Ar}$ differently than natural
404 fugitive gas loss during bubble close-off. Omitting the gas loss correction indeed makes $^{86}\text{Kr}_{\text{xs}}$ at DF
405 negative (Fig. A3C-D). Another hypothesis is that the positive $^{86}\text{Kr}_{\text{xs}}$ signal is an artefact of the seasonal
406 rectifier that Morgan et al. (2022) identify at DF. In this work we assume a linear approach in which the
407 effect of the rectifier can be described by a single ΔT value that is the same for isotopic pairs. In reality,
408 there may be non-linear interactions between thermal fractionation and firm advection that impact the
409 isotopic values of the various gases in a more complex way than captured in our approach.

410 The $^{86}\text{Kr}_{\text{xs}}$ is also correlated with other site characteristics besides Φ . For site elevation we find $r = 0.96$
411 (0.84); and for mean annual temperature $r = -0.87$ (-0.76); the number in parentheses gives the correlation
412 when using all the individual samples rather than site-mean $^{86}\text{Kr}_{\text{xs}}$. The listed correlations all have $p < 0.01$.
413 For site accumulation we do not find a statistically significant correlation at the 90% confidence level. The
414 correlations with elevation and temperature are comparable to those we find for Φ ; this is no surprise given
415 that elevation, Φ and T are all strongly correlated with one another, mainly because elevation directly
416 controls both T (via the lapse rate) and Φ (by limiting the penetration of storms). To our knowledge there
417 are no mechanisms through which either elevation or annual-mean temperature could drive kinetic isotopic
418 fractionation in the firm layer. Perhaps other unexamined site characteristics (such as the degree of density



419 layering, or the magnitude of the annual temperature cycle) could provide good correlations also, suggesting
420 additional hidden controls on $^{86}\text{Kr}_{\text{xs}}$. The data needed to assess such hidden controls are not available for
421 most sites.

422 The calibration of the $^{86}\text{Kr}_{\text{xs}}$ proxy is based on spatial regression. In applying the proxy relationship to
423 temporal records, we make the implicit assumption that proxy behavior in the temporal and spatial
424 dimensions is at least qualitatively similar. This assumption may prove incorrect. In particular, changes in
425 insolation are known to impact firn microstructure and bubble close-off characteristics, which in turn
426 impacts gas records of $\delta\text{O}_2/\text{N}_2$ and total air content (Bender, 2002; Raynaud et al., 2007). Since $^{86}\text{Kr}_{\text{xs}}$ is
427 linked to the dispersivity of deep firn, it seems probable that insolation has a direct impact on $^{86}\text{Kr}_{\text{xs}}$ also via
428 the firn microstructure. We will revisit this issue in our interpretation of the WD $^{86}\text{Kr}_{\text{xs}}$ record (Section 5).
429 Overall, we anticipate $^{86}\text{Kr}_{\text{xs}}$ to be a qualitative proxy for synoptic variability, yet want to caution against
430 quantitative interpretation based on the spatial regression slope.

431 The observations presented in this section clearly highlight the fundamental shortcomings of our current
432 understanding of firn air transport hinting at the existence of complex interactions, presumably at the pore-
433 scale, that are not being represented. Percolation theory finds that near the critical point (presumably the
434 lock-in depth) a network becomes fractal in its nature; we suggest that this fractal nature of the pore network
435 likely contributes to non-linear pore-scale interactions that give rise to the $^{86}\text{Kr}_{\text{xs}}$ observations in ice. While
436 the observed correlation of Fig. 3C is highly encouraging, further work is critical to understand this proxy.
437 Examples of such future studies are: (1) additional high-resolution records that can resolve the true
438 variations that exist in a single ice core, similar to the DE08-OH record; (2) 3-D firn air transport model
439 studies; (3) improvements to the gas loss correction; (4) additional coring sites to further confirm the
440 validity of the proxy; (5) Adding xenon isotopic constraints (^{136}Xe excess) as an additional marker of
441 isotopic disequilibrium; (6) numerical simulations of pore-scale air transport in large-scale firn networks;
442 (7) experimental studies of dispersion in firn samples; and (8) percolation theory approaches to study the
443 fractal nature of the pore network of the lock-in zone.



444 **4 Present-day controls on Kr-86 excess in Antarctica**

445 In this section we investigate the large-scale patterns of climate variability in the Southern Hemisphere that
446 could affect Φ and therefore $^{86}\text{Kr}_{\text{xs}}$ over Antarctica. We begin by investigating the patterns in the wind field
447 that are associated with changes in Φ at ice core sites, before examining how more canonical patterns of
448 Southern Hemisphere climate variability, such as the southern annular mode (SAM), might affect Φ over
449 the whole of Antarctica.

450 We use ERA-interim reanalysis data for the 1979-2017 period (Dee et al., 2011) to evaluate the present-
451 day controls on synoptic-scale pressure variability in Antarctica. Kr-86 excess in an ice core sample
452 averages over several years of pressure variability, and therefore we focus on annual-mean correlation in
453 our analysis. The annual-mean Φ is calculated from the 6-hourly reanalysis data using Eq. (5). Note that
454 we let the year run from April to March to avoid dividing single El Niño / La Niña events across multiple
455 years.

456 At all Antarctic sites investigated, a similar pattern exists; four representative locations are shown in Fig.
457 4, where we regress the zonal wind in the lower (850 hPa, color shading) and upper troposphere (200 hPa,
458 contours) onto our surface pressure variability parameter Φ . We find that synoptic pressure variability at
459 these sites is linked to zonal winds along the southern margin of the eddy-driven subpolar jet (SPJ), which
460 extends from the surface to the upper troposphere (Nakamura and Shimpo, 2004; Trenberth, 1991). Sites
461 near the ice sheet margin (Figs. 4A, B and D) are most sensitive to the SPJ edge in their sector of Antarctica,
462 whereas interior sites (Fig. 4C) appear sensitive to the overall strength/position of the SPJ. Note that
463 strengthening, broadening or southward shifting of the SPJ all can in principle enhance site Φ .

464 Pressure variability at WDC is furthermore correlated with the strength of the Pacific Subtropical jet (STJ)
465 aloft (solid contour lines centered around 30°S in the Pacific in panel 4A), forming an upper troposphere
466 wind pattern that resembles the wintertime South Pacific split jet (Bals-Elsholz et al., 2001; Nakamura and
467 Shimpo, 2004); this agrees with the finding that a strengthening of the split jet enhances storminess over
468 West Antarctica (Chiang et al., 2014).

469 Next, we investigate how the well-known patterns of large-scale atmospheric variability, such as SAM and
470 ENSO, impact pressure variability in Antarctica. Figure 5 shows the correlation of Φ with the three leading
471 modes of SH extra-tropical atmospheric variability; the correlation with various indices and modes for
472 individual ice core locations is given in Table 2. Most teleconnection patterns have a specific season during
473 which they are strongest; here we do not differentiate between seasons, because $^{86}\text{Kr}_{\text{xs}}$ in ice core samples
474 averages over all seasons.

475 Globally, annual-mean Φ is highest over the Southern Ocean (Fig. 5A); a region of enhanced baroclinicity
476 associated with the eddy-driven SPJ (Nakamura and Shimpo, 2004). The green line denotes the latitude of
477 maximum Φ , corresponding roughly to the latitude with the highest storm track density (57.8°S on average).

478 The dominant mode of atmospheric variability in the SH extratropics is the southern annular mode,
479 representing the vacillation of atmospheric mass between the mid- and high-latitudes (Thompson and
480 Wallace, 2000). Figure 5B shows 500 hPa geopotential height (Z500) anomalies associated with the SAM
481 as contours, with the color shading giving the correlation between Φ and the SAM index. During the



482 positive SAM phase (negative Z500 over Antarctica) we find that the stormtracks and maximum synoptic
483 activity are displaced towards Antarctica (positive Φ correlation poleward of the green line in Fig. 5B).
484 This is associated with a strengthening and poleward displacement of the SH westerly winds that occurs
485 during a positive SAM phase. More locally, Φ on the Antarctic Peninsula is positively correlated with the
486 SAM-index (Table 2); Φ at the other sites is not meaningfully impacted. This suggests that the variations
487 associated with the SAM (as commonly defined) do not extend far enough poleward to meaningfully impact
488 Antarctica with the exception of the Peninsula. Enhanced synoptic variability on the Peninsula during
489 positive SAM phases is consistent with observations of enhanced snowfall at those times (Thomas et al.,
490 2008).

491 The second mode of SH extratropical variability is the Pacific-South American Mode 1 (PSA1), which
492 reflects a Rossby wave response to sea surface temperature (SST) anomalies over the central and eastern
493 equatorial Pacific (Mo and Paegle, 2001), and is therefore closely linked to ENSO on interannual time
494 scales (we find a correlation of $r = 0.77$ between the annual mean PSA1 and Niño 3.4 indices). Φ in the
495 Amundsen and Ross Sea sectors (WDC, SDM and RICE) is positively correlated to the PSA1 and Niño 3.4
496 SST, suggesting larger synoptic activity during El Niño phases and low activity during La Niña phases. The
497 PSA2 pattern, also linked to SST anomalies in the tropical Pacific (Mo and Paegle, 2001), is likewise
498 correlated to Φ in the Amundsen and Ross Sea sectors (Fig. 5C and Table 2). While all the correlations
499 listed are statistically significant, they explain only a fraction of the total variability.

500 Next, we consider anomalies in sea ice area and extent (Parkinson and Cavalieri, 2012). We focus on the
501 Ross and Amundsen-Bellingshausen Seas where impacts on WAIS Divide may be expected. At the 90%
502 confidence level we do not find significant correlations to sea ice area or extent at most core locations
503 (Table 2). Correlations to sea ice extent are (even) weaker than those for sea ice area and consequently not
504 shown. We performed a lead-lag study of the correlations between Φ and sea ice area/extent in the various
505 sectors, and find that in all cases maximum correlations occur for the sea ice changes lagging 0 to 4 months
506 behind Φ ; we interpret this to mean that the sea ice is responding to changes in atmospheric circulation,
507 rather than driving them.

508 Overall, we find that synoptic activity at WAIS Divide, the site of most interest here, is controlled by the
509 position and/or strength of the stormtracks at the southern edge of the SPJ in the Pacific sector of the
510 Southern Ocean (Ross, Amundsen and Bellingshausen Seas), with little sensitivity to the SPJ behavior in
511 the other sectors. Owing to its remote southern location, WDC is only weakly impacted by the commonly-
512 defined large-scale modes of atmospheric variability. Most notably, WDC has a modest influence from the
513 tropical Pacific climate, as shown by a correlation around $r \approx 0.3$ to the PSA1, Niño 3.4 and PDO indices
514 (Table 2). We further find statistically significant correlations (up to $r = 0.44$) between WDC Φ and SST
515 in broad regions of the central and eastern tropical Pacific (not shown). We suggest that ENSO weakly
516 impacts storminess at WDC (around 10% of variance explained) via its impact on the SPJ in the South
517 Pacific.



518 **5 Barometric variability in West Antarctica during the last deglaciation**

519 **5.1 The 0-24 ka WAIS Divide Kr-86 excess record**

520 The WAIS Divide downcore $^{86}\text{Kr}_{\text{xs}}$ dataset we present here was produced during five separate measurement
521 campaigns that occurred in February-April 2014, February-April 2015, August 2015, August 2020, and
522 August 2021, respectively. Campaigns 1-3 were reported previously (Bereiter et al., 2018a; Bereiter et al.,
523 2018b), and campaigns 4 and 5 were meant to resolve conflicts between the $^{86}\text{Kr}_{\text{xs}}$ data sets from these
524 earlier campaigns. Three slightly different measurement approaches were used. Campaign 1 uses “Method
525 1” from Bereiter et al. (2018a), in which the air sample splitting is done in a water bath for over 12 hours
526 to equilibrate the sample. Campaigns 2 and 3 use “Method 2” from Bereiter et al. (2018a), in which a
527 bellows is used to split the air samples for over 4 to 6 hours. Campaigns 4 and 5 do not involve splitting of
528 the air sample, and only analyzed the Kr and Ar isotopic ratios. During campaign 4 a glass bead from the
529 water trap had gotten stuck in the tubing, restricting the flow and likely resulting in incomplete air extraction
530 from the melt water.

531 Figure 6 compares $^{86}\text{Kr}_{\text{xs}40}$ (panel A) and $^{86}\text{Kr}_{\text{xs}15}$ (panel B) from the five campaigns. Campaign 1 is the
532 only campaign that spans the full age range of the record, making it the most valuable of the three
533 campaigns. Campaigns 2 and 3 are mostly restricted to the Pleistocene and Holocene periods respectively,
534 with little overlap between them. Campaigns 4 and 5 aimed to reproduce some of the most salient features
535 in the earlier three.

536 No true replicate samples were analyzed between the campaigns, in part because the large sample size
537 requirement precludes this. To assess offsets, we rely on nearest-neighbor linear interpolation. We find an
538 offset of 5 per meg between the first and second campaign (during their period of overlap); this is within
539 the analytical precision (22 per meg), suggesting these two campaigns are in good agreement. The
540 agreement is good for both the $^{86}\text{Kr}_{\text{xs}40}$ and $^{86}\text{Kr}_{\text{xs}15}$ definitions. The first downcore campaign furthermore
541 overlaps in depth with the WDC calibration dataset (gray data in Fig. 6); we find no offset between those
542 data sets either. Data from campaign 2 appear to have more scatter, possibly reflecting the shorter
543 equilibration time during sample splitting.

544 We combine data from the first two campaigns, and evaluate their offset to data from the other three
545 campaigns using nearest-neighbor linear interpolation. For campaigns 3, 4 and 5 we find an offset of -31,
546 -22 and -23 per meg ‰^{-1} in $^{86}\text{Kr}_{\text{xs}40}$, respectively. For campaign 3 the offset is -34 per meg ‰^{-1} in $^{86}\text{Kr}_{\text{xs}15}$.
547 It is remarkable that all three later campaigns are more negative in $^{86}\text{Kr}_{\text{xs}}$ than the first two. Campaign 3
548 shows the greatest offset (greater than analytical precision), and has more scatter in both $^{86}\text{Kr}_{\text{xs}}$ (Fig. 6) and
549 ^{15}N excess (Fig. A5), and less care was taken during this campaign that the IRMS conditions were stable.
550 The offset of campaign 4 may be attributed to the incomplete sample transfer due to the bead stuck in the
551 line. The offset in campaign 5 is hard to explain. The systematically more negative $^{86}\text{Kr}_{\text{xs}}$ of campaigns 4
552 and 5 may reflect sample storage effects, as these were measured 5-6 years after campaign 1 and 2. However
553 this would not explain the negative values of campaign 3. The good $^{86}\text{Kr}_{\text{xs}}$ agreement between DE08 and
554 DE08-OH, drilled 32 years apart, would also argue against large storage effects. For campaign 4 and 5 only
555 Ar and Kr isotope ratios were measured, and so we lack typical tracers of gas loss ($\delta\text{O}_2/\text{N}_2$ and $\delta\text{Ar}/\text{N}_2$)



556 In the remainder of this paper we will interpret the combined data from campaigns 1 and 2, but with the
557 caveat that there is a persistent offset with later campaigns. However, the features we interpret are
558 corroborated by the later campaigns, if one takes the offset into account. To aid interpretation of the data,
559 we apply a Gaussian smoothing spline with a smoothing filter width that varies depending on the data
560 density (from 250-year width in the deglaciation itself where the data density is high, to 1750 years in the
561 Holocene and LGM where data density is low). To estimate the uncertainty in the smoothing spline we use
562 a Monte Carlo approach that considers uncertainty in (1) the gas loss correction, by randomly sampling ϵ_{40}
563 in the range of 0 to -0.008; (2) the thermal correction, by randomly scaling the thermal scenario (Fig. A5)
564 by a factor ranging from 0 to 2; and (3) analytical errors, by adding random errors to individual data points
565 drawn from a normal distribution with a 2σ width of 22 per meg. The $\pm 1\sigma$ uncertainty range with mean
566 value are shown as the gray envelope and center line in Fig. 6. We believe the following observations to be
567 robust:

- 568 • The Holocene shows a trend towards increasingly negative $^{86}\text{Kr}_{\text{xs}}$, suggesting a gradual increase in
569 synoptic activity toward the present. Minimum synoptic activity in West Antarctica occurs during the
570 early Holocene around 10 ka BP; the Monte Carlo study suggests $^{86}\text{Kr}_{\text{xs}40}$ in the early Holocene (8ka-
571 10ka BP) is 30.5 ± 18 per meg ‰^{-1} ($\pm 2\sigma$) below the late-Holocene value (last 2 ka). Using the slope of
572 our core-top calibration (Fig. 3), we estimate that early-Holocene WDC synoptic activity Φ is $\sim 17\%$
573 weaker than it is today. This change is comparable to the 2σ magnitude of interannual variations in
574 annual mean Φ at the site today (or about half the peak-to-peak variations thereof). This Holocene trend
575 is seen in the data from campaigns 1, 3 and 4; campaign 5 does not suggest a trend but has only one
576 late Holocene data point making it less robust.
- 577 • The most pronounced change occurs at the Younger Dryas (YD) - Holocene transition, where $^{86}\text{Kr}_{\text{xs}}$
578 becomes more positive (by 30.1 ± 16 per meg ‰^{-1} , comparing YD and early Holocene) implying a
579 decrease in synoptic activity. This transition is observed in campaigns 1, 2, 4 and 5 that cover this time
580 period (the third campaign does not cover it), and represents a $\sim 17\%$ drop in synoptic activity (Φ).
- 581 • During the Last Glacial Maximum (LGM), WDC synoptic activity was perhaps slightly weaker than at
582 present, but not significantly so ($^{86}\text{Kr}_{\text{xs}40}$ more positive by 11 ± 13 per meg ‰^{-1}). The West Antarctic
583 ice sheet elevation was likely higher during the LGM, and a 300 m elevation increase would by itself
584 increase $^{86}\text{Kr}_{\text{xs}40}$ by 10 per meg ‰^{-1} , all else being equal (Appendix A3). This feature is seen in
585 campaign 1 and not covered by the other campaigns.
- 586 • The deglaciation itself has enhanced synoptic activity, in particular during the two North-Atlantic cold
587 stages Heinrich Stadial 1 (HS1) and the YD as highlighted with yellow bars in Figs. 6 and 7. Synoptic
588 activity during these periods is enhanced relative to the adjacent LGM and early Holocene, yet
589 comparable to today. This feature is seen in campaigns 1 and 2, and in 4 and 5 for the transition into
590 the Holocene.

591 Below we will interpret the deglacial WD $^{86}\text{Kr}_{\text{xs}}$ record in terms of barometric variability. Before doing so
592 we want to emphasize that firn processes may have been imprinted onto the record also, in particular on
593 orbital timescales where firn microstructure responds to local (summer) insolation intensity (Bender, 2002).
594 High summer insolation results in more depleted $\delta\text{O}_2/\text{N}_2$ and reduced air content, likely via stronger
595 layering and a delayed pore close-off process (Fujita et al., 2009).



596 Local summer solstice insolation in Antarctica increases through the Holocene, with the highest values in
597 the late Holocene. This may impact $^{86}\text{Kr}_{\text{xs}}$, although it is not a-priori clear what the sign of this relationship
598 would be. The sense of the Holocene temporal trends is that a more negative $^{86}\text{Kr}_{\text{xs}}$ coincides with more
599 negative $\delta\text{O}_2/\text{N}_2$. Note that this is opposite to the trends seen in the spatial calibration, where sites with the
600 most negative $\delta\text{O}_2/\text{N}_2$ (DF, SP, EDC) have the most positive $^{86}\text{Kr}_{\text{xs}}$. For now, the impact of local insolation
601 on $^{86}\text{Kr}_{\text{xs}}$ via firm microstructure remains unknown, which is an important caveat in interpreting the orbital-
602 scale changes in WD $^{86}\text{Kr}_{\text{xs}}$. The abrupt $^{86}\text{Kr}_{\text{xs}}$ increase at the Holocene onset is too abrupt to be caused by
603 insolation changes, and thus we can interpret that change with more confidence.

604 **5.2 Barometric variability at WAIS Divide during the last deglaciation**

605 In the present-day, synoptic-scale pressure variability at WAIS Divide is correlated with zonal wind
606 strength along the southern margin of the SPJ (Section 4). In our interpretation, a more negative $^{86}\text{Kr}_{\text{xs}}$
607 reflects a strengthening or southward shift of the SPJ in the Pacific sector. Here we provide a climatic
608 interpretation of the deglacial WDC $^{86}\text{Kr}_{\text{xs}}$ record, and suggest that variations in synoptic variability at WDC
609 are linked to meridional movement of the ITCZ on millennial and orbital timescales.

610 The main features of the deglacial WDC $^{86}\text{Kr}_{\text{xs}}$ record listed in Section 5.1 resemble similar features seen
611 in records of (sub-) tropical hydrology and monsoon strength, such as the speleothem calcite $\delta^{18}\text{O}$ records
612 from Hulu Cave, China (Fig. 7C) and from Botuvera cave, southern Brazil (Fig. 7D), which are thought to
613 reflect the intensity of the East Asian and South American summer monsoons, respectively (Cruz et al.,
614 2005; Wang et al., 2007; Wang et al., 2001). These two monsoon records are anti-correlated, showing
615 opposing rainfall trends between the NH and SH on both orbital and millennial timescales. This pattern is
616 commonly attributed to displacement of the mean meridional position of the ITCZ (Chiang and Friedman,
617 2012; McGee et al., 2014; Schneider et al., 2014), driven by hemispheric temperature differences (Fig. 7B).
618 On orbital timescales such ITCZ migration has a strong precessional component, moving towards the
619 hemisphere with more intense summer peak insolation; on millennial timescales the ITCZ responds to
620 abrupt North-Atlantic climate change associated with the D-O and Heinrich cycles (Broccoli et al., 2006;
621 Chiang and Bitz, 2005; Wang et al., 2001), which are in turn linked to changes in meridional heat transport
622 by the Atlantic meridional overturning circulation, or AMOC (Lynch-Stieglitz, 2017; Rahmstorf, 2002).

623 Changes in mean ITCZ position have a strong influence on the structure and strength of the SH jets. During
624 periods when the NH is relatively cold (such as D-O stadials or periods with negative orbital precession
625 index) the ITCZ is displaced southward and the SH Hadley cell is weakened, thereby also weakening the
626 SH upper-tropospheric subtropical jet (Ceppi et al., 2013; Chiang et al., 2014). The reverse is also true, with
627 the ITCZ shifted northward during NH warmth, associated with a strengthening of the SH Hadley cell and
628 STJ. In a range of model simulations (Ceppi et al., 2013; Lee and Kim, 2003; Lee et al., 2011; Pedro et al.,
629 2018) the weakening of the SH STJ (as during NH cold) is furthermore accompanied by a strengthening
630 and/or southward shift of the SPJ/eddy-driven jet and SH westerly winds. Recently, ice core observations
631 have confirmed in-phase shifts in the position of the SHW occur during the D-O cycle in parallel to those
632 of the ITCZ (Buizert et al., 2018; Markle et al., 2017). Marine records of fluvial sediment runoff off the
633 Chilean coast suggest precession-phased movement of the South Pacific SPJ, again in parallel to the ITCZ
634 movement (Lamy et al., 2019).



635 While data and models thus appear to agree on this first-order zonal-mean circulation response, zonal
636 asymmetries may lead to divergent outcomes at individual locations, particularly in the Pacific sector of
637 Antarctica where WDC is located. While the Heinrich (i.e. NH cooling) simulations clearly show the
638 aforementioned zonal-mean strengthening of the eddy-driven jet (Lee et al., 2011), they also suggest a
639 weakening of the South Atlantic austral winter split jet (Chiang et al., 2014); in this weakened split jet
640 configuration the STJ and SPJ are weakened at the expense of a strengthened mid-latitude jet. Essentially
641 the literature presents us with two opposing hypotheses for the response of the South Pacific SPJ to ITCZ
642 migration. In the zonal-mean framework, meridional ITCZ migration is accompanied by a parallel shift
643 (and/or strengthening) of the SH SPJ/eddy-driven jet, suggesting an anti-correlation between ITCZ latitude
644 and Antarctic storminess (with weak synoptic activity as the ITCZ is shifted north). However, if zonal
645 asymmetries in the SPJ response are considered, storminess at WDC may actually have the opposite
646 relationship to ITCZ position, due to a proposed weakening (strengthening) of the split jet as the ITCZ
647 shifts south (north). Our $^{86}\text{Kr}_{\text{xs}}$ record implies that synoptic activity at WDC is anticorrelated with ITCZ
648 position, suggesting that the zonally symmetric SPJ response advocated by e.g. Ceppi et al. (2013)
649 dominates over the zonally asymmetric split jet response advocated by Chiang et al. (2014).

650 The present-day SAM is sometimes suggested as an analogue for past shifts in the meridional position of
651 the SHW and eddy-driven jet (Rind et al., 2001); during positive SAM phases the SHW are displaced
652 poleward, and during negative phases equatorward. The WDC Kr-86 excess record, combined with our
653 analysis of the present-day circulation (Fig. 4), implies changes to the position and/or strength of the
654 southern edge of the SPJ. However, we find that the present-day SAM does not have a statistically
655 significant impact on synoptic variability at WDC (Table 2). Perhaps the SAM is not a good analogue for
656 these past changes in circulation after all, in particular when considering the impact of SHW shifts on
657 Antarctic storminess. The present-day SAM represents a mode of internal variability, with anomalies
658 persisting for only weeks to months – the timescale is longest in late spring and early summer reflecting a
659 stronger planetary wave–mean flow interaction (Simpson et al., 2011; Thompson and Wallace, 2000). By
660 contrast, the shifts in the ITCZ, and presumably the associated changes to the SH jet structure, persist for
661 centuries to millennia. Moreover, the atmospheric dynamics of the SAM and the ITCZ-driven shifts in the
662 SHW are very different, with the latter being driven from the tropics via hemispherically asymmetric
663 changes in Hadley cell and STJ strength. At first glance it may appear contradictory to state, as we do, that
664 synoptic activity at WDC is not sensitive to the SAM while also suggesting that during the last deglaciation
665 synoptic activity at WDC is linked to changes in the position of the SH eddy-driven jet and westerlies.
666 Based on the considerations above, both claims may be true without contradiction.

667 Besides secular changes to the SPJ position/strength linked to meridional ITCZ movement, WDC $^{86}\text{Kr}_{\text{xs}}$
668 may also have imprints from ENSO and tropical Pacific climate. Our analysis suggests a weak, but
669 statistically significant link to common ENSO indicators (Table 2). Increased synoptic activity at WDC is
670 linked to enhanced convection in the central and eastern tropical Pacific, which may be due to enhanced
671 frequency or intensity of El Niño events, or a mean climate state that is more El Niño-like; it seems likely
672 that the Pacific mean state and ENSO variability are strongly linked (Salau et al., 2012), and the distinction
673 may be irrelevant.

674 The key features of the WDC $^{86}\text{Kr}_{\text{xs}}$ record are compatible with paleo-ENSO changes commonly described
675 in the literature. A majority of Holocene ENSO reconstructions (Conroy et al., 2008; Driscoll et al., 2014;
676 Koutavas et al., 2006; Moy et al., 2002; Riedinger et al., 2002; Sadekov et al., 2013) and a wide range of



677 climate model simulations (Braconnot et al., 2012; Cane, 2005; Clement et al., 2000; Liu et al., 2000; Liu
678 et al., 2014; Zheng et al., 2008) all suggest weakened ENSO activity during the early and mid-Holocene, a
679 time with reduced WDC synoptic activity. For example, Fig. 7F shows the number of El Niño events per
680 century (with trend line) reconstructed from inorganic clastic laminae in sediments from Laguna
681 Pallcacocha, Ecuador, a region strongly affected by ENSO (Moy et al., 2002). Likewise, it has been
682 suggested that the SST gradient between the West Pacific warm pool and East Pacific cold tongue was
683 enhanced during the mid-Holocene, perhaps indicating a more La Niña-like mean climate state (Koutavas
684 et al., 2002; Sadekov et al., 2013).

685 Going from the early Holocene to the Younger Dryas (YD), we observe a large increase in WDC synoptic
686 activity. Enhanced ENSO activity during Heinrich stadials is generally supported by climate model
687 simulations (Braconnot et al., 2012; Merkel et al., 2010; Timmermann et al., 2007), and by limited proxy
688 evidence for stadial periods more broadly (Stott et al., 2002). Enhanced ENSO variability during the
689 deglaciation is also found by Sadekov et al. (2013), although their record lacks the temporal resolution to
690 resolve the individual stages. The zonal SST gradient in the equatorial Pacific further reaches a minimum
691 during HS1, also consistent with higher El Niño intensity (Sadekov et al., 2013).

692 The observed variations in $^{86}\text{Kr}_{\text{xs}}$ and implied changes in WDC synoptic activity may thus have two
693 contributions: (1) ITCZ-driven changes to the South Pacific SPJ position, and (2) changes to ENSO activity.
694 Based on previous work, we argue these two amplify one another in driving WDC storminess, yet we expect
695 the former to make the larger contribution. To disentangle zonally-uniform changes to the SPJ from changes
696 specific to the Pacific sector (such as ENSO and the split jet), $^{86}\text{Kr}_{\text{xs}}$ records from different sectors of
697 Antarctica are needed. Replication of the deglacial and Holocene WDC $^{86}\text{Kr}_{\text{xs}}$ record presented here is also
698 a high priority, both at WDC itself and at the nearby SDM and RICE cores, to validate that the signals we
699 describe and interpret here are indeed real and regional in scale.

700 The position of the SHW during the LGM has been a topic of much scientific inquiry. Proxy data have been
701 interpreted to show a northward LGM shift of the SHW – with other scenarios, including no change at all,
702 not excluded by the data (Kohfeld et al., 2013). Such a shift is not supported by most climate models (Rojas
703 et al., 2009; Sime et al., 2013). Our $^{86}\text{Kr}_{\text{xs}}$ record suggests LGM synoptic activity in West Antarctica to be
704 comparable to today after accounting for site elevation effects. This would be consistent with a Pacific SPJ
705 position similar to today. Note that our site is mostly sensitive to the position of the southern edge of the
706 SPJ, and cannot meaningfully constrain changes to the seasonality, width, and/or northern edge of the
707 stormtracks. Therefore, it is not a-priori clear whether our observations can be extrapolated to more general
708 statements about SHW position and strength during the LGM. Our data suggest that SPJ movement follows
709 insolation and the ITCZ position, and hence the LGM period may not be a good target for studying SHW
710 movement in the first place given that it has a precession index similar to the present-day.

711 Changes to the SPJ and its associated westerly surface winds have implications for ocean circulation and
712 marine productivity in the Southern Ocean via wind-driven upwelling. Opal flux records from the Antarctic
713 zone (Fig. 7G), reflecting diatom productivity, are commonly interpreted as a proxy for such upwelling –
714 with enhanced upwelling during southward displacement of the SHW (Anderson et al., 2009). Here we
715 only show records from the Pacific sector, given we find WDC $^{86}\text{Kr}_{\text{xs}}$ to reflect purely local SPJ dynamics
716 (Fig. 4A). Both published records suggest enhanced upwelling during the deglaciation (Fig. 7G), consistent
717 with a southward-shifted Pacific SPJ and enhanced storminess at WDC. The record from core PS75/072-4



718 (blue curve) further indicates an increasing productivity trend through the Holocene (Studer et al., 2018),
719 which is accompanied by a rise in surface nitrogen availability (reconstructed from diatom-bound nitrogen
720 isotopic composition, not shown); this Holocene trend matches our finding of increasing WDC storminess
721 and, by inference, an increasingly southern position of the Pacific SPJ and SHW. We thus conclude that
722 our interpretation of WDC $^{86}\text{Kr}_{\text{xs}}$ reflecting SPJ movement in parallel with the ITCZ, is broadly consistent
723 with indicators of wind-driven upwelling in the Pacific Antarctic zone.



724 6 Conclusions

725 Here we present and calibrate a new gas-phase ice core climate proxy, Kr-86 excess, that reflects time-
726 averaged surface pressure variability at the site driven by synoptic activity. Surface pressure variability
727 weakly disturbs the gravitational settling and enrichment of the noble gas isotope ratios $\delta^{86}\text{Kr}$ and $\delta^{40}\text{Ar}$ via
728 barometric pumping. Owing to its higher diffusion coefficient, argon is less affected by this process than
729 krypton is, and therefore the difference $\delta^{86}\text{Kr}-\delta^{40}\text{Ar}$ is a measure of synoptic activity.

730 This interpretation is supported by a calibration study in which we measure $^{86}\text{Kr}_{\text{xs}}$ in late Holocene ice core
731 samples from eleven Antarctic and one Greenland ice core that represent a wide range of synoptic activity
732 in the modern climate. Two of the Antarctic cores were rejected due to clear evidence of refrozen melt
733 water. We find a strong correlation ($r = -0.94$ when using site mean data and $r = -0.83$ when using individual
734 samples, $p < 0.01$) between ice core $^{86}\text{Kr}_{\text{xs}}$ and barometric variability at the site, demonstrating the validity
735 of the new proxy.

736 Current limitations of the new $^{86}\text{Kr}_{\text{xs}}$ proxy are: (1) it requires relatively large and non-trivial corrections
737 for gas loss and thermal fractionation; (2) it is moderately sensitive to changes in convective zone thickness;
738 (3) firn air transport models cannot simulate the magnitude of $^{86}\text{Kr}_{\text{xs}}$ anomalies measured in ice samples;
739 (4) firn air samples show smaller $^{86}\text{Kr}_{\text{xs}}$ anomalies than ice samples from the same site do; (5) it may be
740 sensitive to the degree of density layering at the site, as a comparison of the nearby Law Dome DE08 and
741 DSSW20K cores suggests; (6) it does not work for warm sites that experience frequent melt; (7) the
742 measurement is challenging (with offsets observed between measurement campaigns), time consuming,
743 and needs large ice samples; and (8) long-term sample storage may impose data offsets.

744 Using atmospheric reanalysis data, we show that synoptic-scale barometric variability in Antarctica is
745 primarily linked to the position and/or strength of the southern edge of the eddy-driven subpolar jet (SPJ,
746 also called polar front jet) with a southward SPJ displacement enhancing synoptic-scale surface pressure
747 variability in Antarctica. The commonly-defined modes of large-scale atmospheric variability, such as the
748 southern annular mode and the Pacific-South American pattern, impact Antarctic only weakly as they are
749 weighted towards the mid-latitudes; the exception is the Antarctic Peninsula, where synoptic activity is
750 well-correlated with the southern annular mode ($r = 0.68$). Sites in the Amundsen and Ross Sea sectors are
751 weakly linked to tropical Pacific climate and ENSO ($r = 0.31$ to $r = 0.43$).

752 We present a new record of $^{86}\text{Kr}_{\text{xs}}$ from the WAIS Divide ice core in West Antarctica, that covers the last
753 24ka including the LGM, deglaciation and Holocene. West Antarctic synoptic activity is slightly below
754 modern levels during the last glacial maximum (LGM); increases during the Heinrich Stadial 1 and Younger
755 Dryas North Atlantic cold periods; weakens abruptly at the Holocene onset; remains low during the early
756 and mid-Holocene (up to $\sim 17\%$ below modern), and gradually increases to its modern value. The WDC
757 $^{86}\text{Kr}_{\text{xs}}$ record resembles records of tropical hydrology and monsoon intensity that are commonly thought to
758 reflect the meridional position of the ITCZ; the sense of the correlation is that WDC synoptic activity is
759 weak when the ITCZ is in its northward position, and vice versa. We interpret the record to reflect
760 migrations of the eddy-driven SPJ in parallel with those of the ITCZ (Ceppi et al., 2013). Secondary
761 influences may come from tropical Pacific climate and ENSO activity. Our $^{86}\text{Kr}_{\text{xs}}$ record is consistent with
762 weakened ENSO activity (or a more La Niña-like mean state) during the mid- and early Holocene, and
763 enhanced ENSO activity during NH stadial periods – both these features have been described in the paleo-



764 ENSO literature. The inferred changes to the SPJ are broadly consistent with proxies that indicate enhanced
765 wind-driven upwelling in the Pacific Antarctic zone during NH cold stadial periods.

766 Kr-86 excess is a new and potentially useful ice core proxy with the ability to enhance our understanding
767 of past atmospheric circulation. More work to better understand this proxy is warranted, and presently the
768 conclusions of this paper should be considered as tentative. In particular, replication of the deglacial Kr-86
769 excess record presented here in nearby cores is needed before these results can be interpreted with
770 confidence. Despite the many challenges of Kr-86 excess, its further development is worthwhile owing to
771 the dearth of available proxies for reconstructing SH extratropical atmospheric circulation.



772 Appendix A: data corrections

773 A1 Gas loss correction

774 Gas loss processes artificially enrich the $\delta^{40}\text{Ar}$ isotopic ratio used to calculate $^{86}\text{Kr}_{\text{xs}}$ (Kobashi et al., 2008b;
775 Severinghaus et al., 2009; Severinghaus et al., 2003). Figure A1B shows the relationships between the two
776 most common gas loss proxies $\delta\text{O}_2/\text{N}_2$ and $\delta\text{Ar}/\text{N}_2$ for all samples in the calibration dataset; we find a slope
777 close to the 2:1 slope commonly reported in the literature (Bender et al., 1995); the exception is the DE08-
778 OH site where the data fall on a 1:1 slope. Depletion in fugitive gases (such as O_2 and Ar) represents the
779 sum of losses during bubble closure in the firn (Bender, 2002; Huber et al., 2006; Severinghaus and Battle,
780 2006), and those during drilling, handling, storage, and analysis of the samples (Ikeda-Fukazawa et al.,
781 2005). The patterns are inconsistent with storage conditions alone – for example the DF and EDC cores
782 were stored very cold and SP drilled very recently; yet all three have strong $\delta\text{O}_2/\text{N}_2$ and $\delta\text{Ar}/\text{N}_2$ depletion.
783 Natural gas loss from the firn, as well as artefactual loss during drilling likely dominate the signal. The
784 DE08-OH samples were dry-drilled and suffered from poor ice quality for the most depleted samples, which
785 may explain the alternate 1:1 slope at the site (Appendix B); note though that a recent work suggests a ~5:1
786 slope for post-coring gas loss (Oyabu et al., 2021).

787 Severinghaus et al. (2009) hypothesize that the apparent 2:1 slope of $\delta\text{O}_2/\text{N}_2$ to $\delta\text{Ar}/\text{N}_2$ depletion is a
788 combination of two mechanisms: size-dependent fractionation during diffusion through the ice lattice, and
789 mass-dependent fractionation (such as molecular or Knudsen diffusion) within ice fractures. In this
790 interpretation, the exact slope would depend on the relative contribution of each process to the total gas
791 loss. It is improbable that both processes would occur in the same ratio at such a wide variety of sites; the
792 2:1 slope is thus more likely an attribute of the gas diffusion rate of gases through ice itself, which is strongly
793 size-dependent, and weakly mass-dependent (Battle et al., 2011).

794 Gas loss is well known to enrich ice samples in $\delta^{18}\text{O}-\text{O}_2$, and following Severinghaus et al. (2009) we plot
795 $\delta^{18}\text{O}$ (corrected for gravity and small atmospheric $\delta^{18}\text{O}_{\text{atm}}$ variations) against gravitationally-corrected
796 $\delta\text{O}_2/\text{N}_2$ in Fig. A1C. We find a slope of 3.5 per meg enrichment in $\delta^{18}\text{O}$ per ‰ of $\delta\text{O}_2/\text{N}_2$ gas loss. This is
797 less than values reported elsewhere (Severinghaus et al., 2009), but provides further evidence for mass-
798 dependent fractionation during gas loss. Our core top dataset further suggests a correlation between
799 $\delta^{40}\text{Ar} - 4 \times \delta^{15}\text{N}$ (a measure of $\delta^{40}\text{Ar}$ enrichment impacted by both thermal fractionation and gas loss) and
800 gravitationally corrected $\delta\text{Ar}/\text{N}_2$ (Fig. A1D), suggesting Ar loss leads to enrichment of the remaining $\delta^{40}\text{Ar}$.

801 Following Severinghaus et al. (2009), we assume that the $\delta^{40}\text{Ar}$ correction scales with gas loss indicator
802 ($\delta\text{O}_2/\text{N}_2 - \delta\text{Ar}/\text{N}_2$):

$$803 \quad \Delta_{GL}^{40} = \epsilon_{40} \times (\delta\text{O}_2/\text{N}_2 - \delta\text{Ar}/\text{N}_2)|_{\text{gravcorr}} \quad (\text{A1})$$

804 with Δ_{GL}^{40} the isotopic gas loss correction on $\delta^{40}\text{Ar}$ and ϵ_{40} a scaling parameter. Note that gravitationally
805 corrected $\delta\text{O}_2/\text{N}_2$ and $\delta\text{Ar}/\text{N}_2$ data are used. Here we rely on data from the Antarctic Byrd ice core for a best
806 estimate of ϵ_{40} (Fig. A2); some samples from this core suffered extreme gas loss with $(\delta\text{O}_2/\text{N}_2 - \delta\text{Ar}/\text{N}_2)$ as
807 low as -100‰. This data set suggest $\epsilon_{40} = -0.008$, or 8 per meg $\delta^{40}\text{Ar}$ enrichment per ‰ of $(\delta\text{O}_2/\text{N}_2 - \delta\text{Ar}/\text{N}_2)$
808 gas loss. Because of the 2:1 slope between $\delta\text{O}_2/\text{N}_2$ and $\delta\text{Ar}/\text{N}_2$, we find that $(\delta\text{O}_2/\text{N}_2 - \delta\text{Ar}/\text{N}_2) \approx \delta\text{Ar}/\text{N}_2$



809 and therefore the coefficient ϵ_{40} would have a similar slope when regressed against $\delta\text{Ar}/\text{N}_2$ instead of
 810 $(\delta\text{O}_2/\text{N}_2 - \delta\text{Ar}/\text{N}_2)$.

811 The value of $\epsilon_{40} = -0.008$ agrees reasonably well with other studies. Kobashi et al. (2008) compare replicate
 812 sample pairs to back out gas loss, and find (statistically significant) correlations between $\delta^{40}\text{Ar}$ enrichment
 813 and $\delta\text{Ar}/\text{N}_2$ (again, which is similar to $\delta\text{O}_2/\text{N}_2 - \delta\text{Ar}/\text{N}_2$). Kobashi et al. (2008) find ϵ_{40} values of -0.006, -
 814 0.005 and +0.007, depending on the depth range and analytical campaign evaluated. The positive value is
 815 surprising, given that most observations, as well as theory, suggest ϵ_{40} should be negative – we consider
 816 this a spurious result given the weak $\delta^{40}\text{Ar} - \delta\text{Ar}/\text{N}_2$ correlation in that particular data set. The other two
 817 values of ϵ_{40} are in reasonable agreement with the Byrd value. For the Siple Dome ice core (Severinghaus
 818 et al., 2003), regressing $\delta^{40}\text{Ar}$ against $\delta\text{Kr}/\text{Ar}$ gives a slope of +0.007; this implies $\epsilon_{40} = -0.007$ in good
 819 agreement with our findings. Last, our coretop data suggest $\delta^{40}\text{Ar}$ enrichment with an ϵ_{40} value of -0.0072
 820 (Fig. A1D), also in good agreement with Byrd.

821 Given the uncertainty in the gas loss parameter, we verify that our results are valid for a wide range of ϵ_{40}
 822 values (Fig. 3B).

823 A2 Thermal correction

824 In the presence of a temperature gradient, thermal diffusion causes isotopic enrichment towards the colder
 825 location. The thermal diffusion sensitivity Ω in units of ‰K^{-1} for the various gases is given as (Grachev
 826 and Severinghaus, 2003a, b; Kawamura et al., 2013):

$$827 \quad \Omega^{15} = \frac{8.656}{T} - \frac{1232}{T^2}$$

$$828 \quad \Omega^{40} = \frac{26.08}{T} - \frac{3952}{T^2}$$

$$829 \quad \Omega^{86} = \frac{5.05}{T} - \frac{580}{T^2}$$

830 We estimate the thermal gradient ΔT in the firn using N-15 excess (Severinghaus et al., 1998):

$$831 \quad \Delta T = \frac{{}^{15}\text{N}_{xs}}{\Omega^{15} - \Omega^{40}/4} = \frac{\delta^{15}\text{N} - (\delta^{40}\text{Ar} + \Delta_{GL}^{40})/4}{\Omega^{15} - \Omega^{40}/4} \quad (\text{A2})$$

832 with Δ_{GL}^{40} the $\delta^{40}\text{Ar}$ gas loss correction from Eq. (A1). Positive values of ΔT indicate that the surface is
 833 warmer than the firn-ice transition. The ΔT then in turn allows us to estimate the thermal corrections:

$$834 \quad \Delta_{TF}^{15} = -\Omega^{15} \Delta T$$

$$835 \quad \Delta_{TF}^{40} = -\Omega^{40} \Delta T$$

$$836 \quad \Delta_{TF}^{86} = -\Omega^{86} \Delta T \quad (\text{A3})$$



837 The samples from the calibration dataset are from the climatically stable late Holocene period, and typically
838 close together in depth; the uncertainty in the ΔT estimation for individual samples therefore exceeds the
839 temporal variability in ΔT . To reduce the uncertainty in the thermal correction we estimate ΔT for individual
840 samples using Eq. (A2), and for each site average the available data to get a site-average firm temperature
841 gradient $\overline{\Delta T}$. The thermal correction is then given by:

$$842 \quad \Delta_{TF}^{15} = -\Omega^{15} \overline{\Delta T}$$

$$843 \quad \Delta_{TF}^{40} = -\Omega^{40} \overline{\Delta T}$$

$$844 \quad \Delta_{TF}^{86} = -\Omega^{86} \overline{\Delta T} \quad (\text{A4})$$

845 The two methods are compared in Figs. A3C (individual sample ΔT) and A3D (site mean $\overline{\Delta T}$); it is clear
846 that the $\overline{\Delta T}$ approach reduces the spread in $^{86}\text{Kr}_{\text{xs}}$ (error bars), but not its mean (white dots). The ΔT estimates
847 in individual samples are subject to errors in the isotopic measurements; some of these errors will cancel
848 out in the $\overline{\Delta T}$.

849 For the downcore WDC record through the deglaciation we can no longer assume a stationary ΔT ; we
850 instead rely on dynamic firm densification model simulations of ΔT (Buizert et al., 2015). A comparison of
851 the simulated and data-based ΔT is shown in Fig. A5 for WDC. The data clearly show a lot more
852 scatter/variability than the simulations do. We interpret this mainly as analytical noise in the $\delta^{15}\text{N}$ and $\delta^{40}\text{Ar}$
853 measurements, however, the gas loss correction (Appendix A1) also impacts the ΔT estimation in individual
854 samples. The comparison suggests that the scatter in the ΔT estimates actually exceeds the magnitude of
855 the simulated thermal signals. Using ΔT of the individual samples would thus introduce much scatter in the
856 (thermally corrected) $^{86}\text{Kr}_{\text{xs}}$ records, and we choose to use the modelled ΔT instead.

857 **A3 Elevation correction**

858 To correct the deglacial WAIS Divide record for elevation changes, we here estimate the $^{86}\text{Kr}_{\text{xs}}$ dependence
859 on site elevation using the calibration dataset. Note that elevation and synoptic activity are strongly
860 correlated for the investigated sites ($r = -0.86$), with synoptic activity decreasing with elevation because
861 the cyclonic systems do not penetrate deeply into the Antarctic interior. Figure A6 shows the result of this
862 exercise. We find a slope of 34 per meg ‰ of $^{86}\text{Kr}_{\text{xs}}$ per 1000 m of elevation change, with a correlation of
863 $r = 0.96$ when considering site-mean $^{86}\text{Kr}_{\text{xs}}$, and $r = 0.86$ when considering individual samples. Note that
864 the GISP2 site is not included in the analysis because it is in Greenland where the elevation- $^{86}\text{Kr}_{\text{xs}}$
865 relationship may be different from Antarctica – it does however fit the Antarctic trend rather well. We
866 further use the simulated WAIS Divide elevation history (Golledge et al., 2014), which simulates an LGM
867 elevation of around 300m higher than at present at WAIS Divide.



868 **Appendix B: Sub-annual $^{86}\text{Kr}_{\text{xs}}$ variations at DE08-OH**

869 The Law Dome DE08-OH site is a revisit of the DE08 site, drilled in the 2018/2019 Austral summer
870 Antarctic field season. We have samples from two separate cores: (1) thirteen 24-cm-long samples from a
871 10-cm-diameter core going from 97 m to 193 m depth at ~ 8 m sample spacing; and (2) eight 6-cm-long
872 samples from a 24-cm-diameter core going from 97.6 m to 99.8 m depth at 30 cm sample spacing. The
873 purpose of the first set was to determine possible long-term variations in $^{86}\text{Kr}_{\text{xs}}$; the purpose of the second
874 set to assess whether there are sub-annual variations in $^{86}\text{Kr}_{\text{xs}}$ due to the seasonality in firn properties and
875 bubble trapping.

876 Both cores were dry-drilled (i.e., no drill liquid was used). The 10-cm-diameter core used was drilled at the
877 beginning of the field season, the 24-cm-diameter core at the end of the field season. Prior to shipment off
878 the continent, both cores were stored in a chest freezer at Casey Station; due to a miscommunication this
879 freezer was set to -20°C rather than -26°C , yet the ice is believed to have stayed below -18°C .

880 Both DE08-OH cores experienced more gas loss than the original DE08 core that we also sampled (Fig.
881 A1 B). In particular the samples from the 10-cm-diameter core were strongly depleted in $\delta\text{Ar}/\text{N}_2$, with the
882 most extreme gas loss seen for the deepest samples where the ice quality was poorest.

883 Fig. B1 shows the high-resolution sub-annual DE08-OH sampling. The data were corrected for gas loss and
884 thermal fractionation, using a site-mean temperature gradient of $\overline{\Delta T} = -1.6^{\circ}\text{C}$, possibly related to a rectifier
885 effect (Morgan et al. 2022). We find strong (5-fold) variations in $^{86}\text{Kr}_{\text{xs}}$ on sub-annual time scales. With an
886 expected annual layer thickness of around 1.3 m at this depth, it appears as though there may be an annual-
887 scale variation in $^{86}\text{Kr}_{\text{xs}}$; the data set has insufficient length to establish this firmly.

888 We refrain from interpreting the long-term variations in $^{86}\text{Kr}_{\text{xs}}$ in the 10-cm-diameter core for two reasons.
889 First, given the strong sub-annual variations seen in the high-resolution sampling, it is unavoidable that we
890 are aliasing the underlying signal in the core. Second, the 10-cm-diameter core suffers from strong gas loss
891 (depleted $\delta\text{Ar}/\text{N}_2$). We attribute this primarily to the dry drilling and imperfect sample storage conditions.
892 Perhaps the greater stresses during drilling a 10-cm core (compared to the 24-cm diameter core) result in
893 more micro-fractures and gas loss.



894 **Supplement**

895 A data supplement is available with this paper.

896 **Data availability**

897 Data are available here: <https://www.usap-dc.org/view/project/p0010037>, and via the data supplement to
898 this paper.

899 **Author contributions**

900 CB, JS, AJS and EJB designed research; SS, AS, BB, KK, DB, AJS, JDM and IO contributed
901 measurements; KK, DME, NB, RLP, RB, EM-T, PDN, DT, and VVP contributed ice core samples; CB
902 and WHGR analyzed reanalysis data; CB, AJS, and BB performed firn modelling; CB drafted the
903 manuscript with input from all authors.

904 **Competing Interests**

905 The authors declare no competing interests.

906 **Acknowledgements**

907 The idea for the Kr-86 excess proxy came out of discussions at the 2014 WAIS Divide Ice Core Science
908 Meeting held at Scripps Institution of Oceanography in La Jolla, CA. The authors want to thank John
909 Chiang, Justin Wettstein, Zanna Chase, Bob Anderson, Tyler Jones and Eric Steig for useful discussions,
910 data sharing and manuscript feedback, the NSF ice core facility (NSF-ICF, formerly the National Ice Core
911 Laboratory) for curating and distributing ice core samples, the European Centre for Medium-Range
912 Weather Forecasts (ECMWF) for making ERA-Interim reanalysis datasets publicly available, and the US
913 ice drilling program for coordinating ice core drilling in Antarctica. Sample collection at Law Dome was
914 supported by the Australian Antarctic Science Program, the Australian Antarctic Division and (at DE08-
915 OH) the U.S. National Science Foundation.

916 **Financial Support**

917 We gratefully acknowledge financial support from the U.S. National Science Foundation (grant numbers
918 ANT-0944343, ANT-1543267, ANT-1543229, ANT-1643716 and ANT-1643669), the New Zealand
919 Ministry of Business, Innovation and Employment (grant numbers RDF-VUW-1103, 15-VUW-131,
920 540GCT32).



921 References

- 922 Anderson, R.F., Ali, S., Bradtmiller, L.I., Nielsen, S.H.H., Fleisher, M.Q., Anderson, B.E. and Burckle, L.H. (2009)
923 Wind-Driven Upwelling in the Southern Ocean and the Deglacial Rise in Atmospheric CO₂. *Science* 323, 1443-
924 1448.
- 925 Baggenstos, D., Häberli, M., Schmitt, J., Shackleton, S.A., Birner, B., Severinghaus, J.P., Kellerhals, T. and Fischer,
926 H. (2019) Earth's radiative imbalance from the Last Glacial Maximum to the present. *Proc. Natl. Acad. Sci. U. S.*
927 *A.*, 201905447.
- 928 Bals-Elsholz, T.M., Atallah, E.H., Bosart, L.F., Wasula, T.A., Cempa, M.J. and Lupo, A.R. (2001) The Wintertime
929 Southern Hemisphere Split Jet: Structure, Variability, and Evolution. *J. Clim.* 14, 4191-4215.
- 930 Battle, M.O., Severinghaus, J.P., Sofen, E.D., Plotkin, D., Orsi, A.J., Aydin, M., Montzka, S.A., Sowers, T. and Tans,
931 P.P. (2011) Controls on the movement and composition of firm air at the West Antarctic Ice Sheet Divide. *Atmos.*
932 *Chem. Phys.* 11, 11007-11021.
- 933 Bender, M., Sowers, T. and Lipenkov, V. (1995) ON THE CONCENTRATIONS OF O-2, N-2, AND AR IN
934 TRAPPED GASES FROM ICE CORES. *J. Geophys. Res.* 100, 18651-18660.
- 935 Bender, M.L. (2002) Orbital tuning chronology for the Vostok climate record supported by trapped gas composition.
936 *Earth Planet. Sci. Lett.* 204, 275-289.
- 937 Bereiter, B., Kawamura, K. and Severinghaus, J.P. (2018a) New methods for measuring atmospheric heavy noble gas
938 isotope and elemental ratios in ice core samples. *Rapid communications in mass spectrometry* 32, 801-814.
- 939 Bereiter, B., Shackleton, S., Baggenstos, D., Kawamura, K. and Severinghaus, J. (2018b) Mean global ocean
940 temperatures during the last glacial transition. *Nature* 553, 39.
- 941 Birner, B., Buizert, C., Wagner, T.J.W. and Severinghaus, J.P. (2018) The influence of layering and barometric
942 pumping on firm air transport in a 2-D model. *The Cryosphere* 12, 2021-2037.
- 943 Braconnot, P., Luan, Y., Brewer, S. and Zheng, W. (2012) Impact of Earth's orbit and freshwater fluxes on Holocene
944 climate mean seasonal cycle and ENSO characteristics. *Clim. Dyn.* 38, 1081-1092.
- 945 Broccoli, A.J., Dahl, K.A. and Stouffer, R.J. (2006) Response of the ITCZ to Northern Hemisphere cooling. *Geophys.*
946 *Res. Lett.* 33, L01702.
- 947 Buizert, C., Cuffey, K.M., Severinghaus, J.P., Baggenstos, D., Fudge, T.J., Steig, E.J., Markle, B.R., Winstrup, M.,
948 Rhodes, R.H., Brook, E.J., Sowers, T.A., Clow, G.D., Cheng, H., Edwards, L.R., Sigl, M., McConnell, J.R. and
949 Taylor, K.C. (2015) The WAIS Divide deep ice core WD2014 chronology - part 1: Methane synchronization (68-
950 31 ka BP) and the gas age-ice age difference. *Climate of the Past* 11, 153-173.
- 951 Buizert, C. and Severinghaus, J.P. (2016) Dispersion in deep polar firm driven by synoptic-scale surface pressure
952 variability. *The Cryosphere* 10, 2099-2111.
- 953 Buizert, C., Sigl, M., Severi, M., Markle, B.R., Wettstein, J.J., McConnell, J.R., Pedro, J.B., Sodemann, H., Goto-
954 Azuma, K., Kawamura, K., Fujita, S., Motoyama, H., Hirabayashi, M., Uemura, R., Stenni, B., Parrenin, F., He,
955 F., Fudge, T.J. and Steig, E.J. (2018) Abrupt ice-age shifts in southern westerly winds and Antarctic climate forced
956 from the north. *Nature* 563, 681-685.
- 957 Buizert, C., Sowers, T. and Blunier, T. (2013) Assessment of diffusive isotopic fractionation in polar firm, and
958 application to ice core trace gas records. *Earth Planet. Sci. Lett.* 361, 110-119.
- 959 Cai, W., Santoso, A., Wang, G., Yeh, S.-W., An, S.-I., Cobb, K.M., Collins, M., Guilyardi, E., Jin, F.-F., Kug, J.-S.,
960 Lengaigne, M., McPhaden, M.J., Takahashi, K., Timmermann, A., Vecchi, G., Watanabe, M. and Wu, L. (2015)
961 ENSO and greenhouse warming. *Nature Clim. Change* 5, 849-859.
- 962 Cane, M.A. (2005) The evolution of El Niño, past and future. *Earth Planet. Sci. Lett.* 230, 227-240.
- 963 Ceppi, P., Hwang, Y.-T., Liu, X., Frierson, D.M.W. and Hartmann, D.L. (2013) The relationship between the ITCZ
964 and the Southern Hemispheric eddy-driven jet. *J. Geophys. Res.* 118, 5136-5146.
- 965 Chase, Z., Anderson, R.F., Fleisher, M.Q. and Kubik, P.W. (2003) Accumulation of biogenic and lithogenic material
966 in the Pacific sector of the Southern Ocean during the past 40,000 years. *Deep Sea Research Part II: Topical Studies*
967 *in Oceanography* 50, 799-832.
- 968 Cheng, H., Edwards, R.L., Sinha, A., Spötl, C., Yi, L., Chen, S., Kelly, M., Kathayat, G., Wang, X., Li, X., Kong, X.,
969 Wang, Y., Ning, Y. and Zhang, H. (2016) The Asian monsoon over the past 640,000 years and ice age terminations.
970 *Nature* 534, 640-646.
- 971 Chiang, J.C. and Friedman, A.R. (2012) Extratropical cooling, interhemispheric thermal gradients, and tropical
972 climate change. *Annu. Rev. Earth Planet. Sci.* 40, 383-412.
- 973 Chiang, J.C.H. and Bitz, C.M. (2005) Influence of high latitude ice cover on the marine Intertropical Convergence
974 Zone. *Clim. Dyn.* 25, 477-496.



- 975 Chiang, J.C.H., Lee, S.-Y., Putnam, A.E. and Wang, X. (2014) South Pacific Split Jet, ITCZ shifts, and atmospheric
976 North–South linkages during abrupt climate changes of the last glacial period. *Earth Planet. Sci. Lett.* 406, 233-
977 246.
- 978 Clement, A.C., Seager, R. and Cane, M.A. (2000) Suppression of El Niño during the Mid-Holocene by changes in the
979 Earth's orbit. *Paleoceanography* 15, 731-737.
- 980 Cobb, K.M., Westphal, N., Sayani, H.R., Watson, J.T., Di Lorenzo, E., Cheng, H., Edwards, R.L. and Charles, C.D.
981 (2013) Highly Variable El Niño–Southern Oscillation Throughout the Holocene. *Science* 339, 67-70.
- 982 Conroy, J.L., Overpeck, J.T., Cole, J.E., Shanahan, T.M. and Steinitz-Kannan, M. (2008) Holocene changes in eastern
983 tropical Pacific climate inferred from a Galápagos lake sediment record. *Quat. Sci. Rev.* 27, 1166-1180.
- 984 Cruz, F.W., Burns, S.J., Karmann, I., Sharp, W.D., Vuille, M., Cardoso, A.O., Ferrari, J.A., Dias, P.L.S. and Viana,
985 O. (2005) Insolation-driven changes in atmospheric circulation over the past 116,000 years in subtropical Brazil.
986 *Nature* 434, 63-66.
- 987 Dee, D.P., Uppala, S.M., Simmons, A.J., Berrisford, P., Poli, P., Kobayashi, S., Andrae, U., Balmaseda, M.A.,
988 Balsamo, G., Bauer, P., Bechtold, P., Beljaars, A.C.M., van de Berg, L., Bidlot, J., Bormann, N., Delsol, C.,
989 Dragani, R., Fuentes, M., Geer, A.J., Haimberger, L., Healy, S.B., Hersbach, H., Hólm, E.V., Isaksen, I., Kållberg,
990 P., Köhler, M., Matricardi, M., McNally, A.P., Monge-Sanz, B.M., Morcrette, J.J., Park, B.K., Peubey, C., de
991 Rosnay, P., Tavolato, C., Thépaut, J.N. and Vitart, F. (2011) The ERA-Interim reanalysis: configuration and
992 performance of the data assimilation system. *Quarterly Journal of the Royal Meteorological Society* 137, 553-597.
- 993 Driscoll, R., Elliot, M., Russon, T., Welsh, K., Yokoyama, Y. and Tudhope, A. (2014) ENSO reconstructions over the
994 past 60 ka using giant clams (*Tridacna* sp.) from Papua New Guinea. *Geophys. Res. Lett.* 41, 6819-6825.
- 995 Dykoski, C.A., Edwards, R.L., Cheng, H., Yuan, D.X., Cai, Y.J., Zhang, M.L., Lin, Y.S., Qing, J.M., An, Z.S. and
996 Revenaugh, J. (2005) A high-resolution, absolute-dated Holocene and deglacial Asian monsoon record from
997 Dongge Cave, China. *Earth Planet. Sci. Lett.* 233, 71-86.
- 998 Emile-Geay, J., Cobb, K.M., Carré, M., Braconnot, P., Leloup, J., Zhou, Y., Harrison, S.P., Corrège, T., McGregor,
999 H.V., Collins, M., Driscoll, R., Elliot, M., Schneider, B. and Tudhope, A. (2015) Links between tropical Pacific
1000 seasonal, interannual and orbital variability during the Holocene. *Nat. Geosci.* 9, 168.
- 1001 Etheridge, D.M., Pearman, G.I. and Fraser, P.J. (1992) CHANGES IN TROPOSPHERIC METHANE BETWEEN
1002 1841 AND 1978 FROM A HIGH ACCUMULATION-RATE ANTARCTIC ICE CORE. *Tellus* 44, 282-294.
- 1003 Fahnestock, M.A., Scambos, T.A., Shuman, C.A., Arthern, R.J., Winebrenner, D.P. and Kwok, R. (2000) Snow
1004 megadune fields on the East Antarctic Plateau: Extreme atmosphere-ice interaction. *Geophys. Res. Lett.* 27, 3719-
1005 3722.
- 1006 Fowler, A.M., Boswijk, G., Lorrey, A.M., Gergis, J., Pirie, M., McCloskey, S.P.J., Palmer, J.G. and Wunder, J. (2012)
1007 Multi-centennial tree-ring record of ENSO-related activity in New Zealand. *Nature Climate Change* 2, 172.
- 1008 Fujita, S., Okuyama, J., Hori, A. and Hondoh, T. (2009) Metamorphism of stratified firn at Dome Fuji, Antarctica: A
1009 mechanism for local insolation modulation of gas transport conditions during bubble close off. *J. Geophys. Res.*
1010 114.
- 1011 Gergis, J.L. and Fowler, A.M. (2009) A history of ENSO events since A.D. 1525: implications for future climate
1012 change. *Clim. Change* 92, 343-387.
- 1013 Gollledge, N.R., Menviel, L., Carter, L., Fogwill, C.J., England, M.H., Cortese, G. and Levy, R.H. (2014) Antarctic
1014 contribution to meltwater pulse 1A from reduced Southern Ocean overturning. *Nat Comm.* 5, 5107.
- 1015 Grachev, A.M. and Severinghaus, J.P. (2003a) Determining the thermal diffusion factor for Ar-40/Ar-36 in air to aid
1016 paleoreconstruction of abrupt climate change. *J. Phys. Chem. A* 107, 4636-4642.
- 1017 Grachev, A.M. and Severinghaus, J.P. (2003b) Laboratory determination of thermal diffusion constants for N-
1018 29(2)/N-28(2) in air at temperatures from -60 to 0 degrees C for reconstruction of magnitudes of abrupt climate
1019 changes using the ice core fossil-air paleothermometer. *Geochim. Cosmochim. Acta* 67, 345-360.
- 1020 Grootes, P.M., Stuiver, M., White, J.W.C., Johnsen, S. and Jouzel, J. (1993) Comparison of oxygen isotope records
1021 from the GISP2 and GRIP Greenland ice cores. *Nature* 366, 552-554.
- 1022 Headly, M.A. and Severinghaus, J.P. (2007) A method to measure Kr/N-2 ratios in air bubbles trapped in ice cores
1023 and its application in reconstructing past mean ocean temperature. *J. Geophys. Res.* 112, 12.
- 1024 Herron, M.M. and Langway, C.C. (1980) Firn densification: An empirical model. *J. Glaciol.* 25, 373-385.
- 1025 Huang, B., Banzon, V.F., Freeman, E., Lawrimore, J., Liu, W., Peterson, T.C., Smith, T.M., Thorne, P.W., Woodruff,
1026 S.D. and Zhang, H.-M. (2014) Extended Reconstructed Sea Surface Temperature Version 4 (ERSST.v4). Part I:
1027 Upgrades and Intercomparisons. *J. Clim.* 28, 911-930.
- 1028 Huber, C., Beyerle, U., Leuenberger, M., Schwander, J., Kipfer, R., Spahni, R., Severinghaus, J.P. and Weiler, K.
1029 (2006) Evidence for molecular size dependent gas fractionation in firn air derived from noble gases, oxygen, and
1030 nitrogen measurements. *Earth Planet. Sci. Lett.* 243, 61-73.



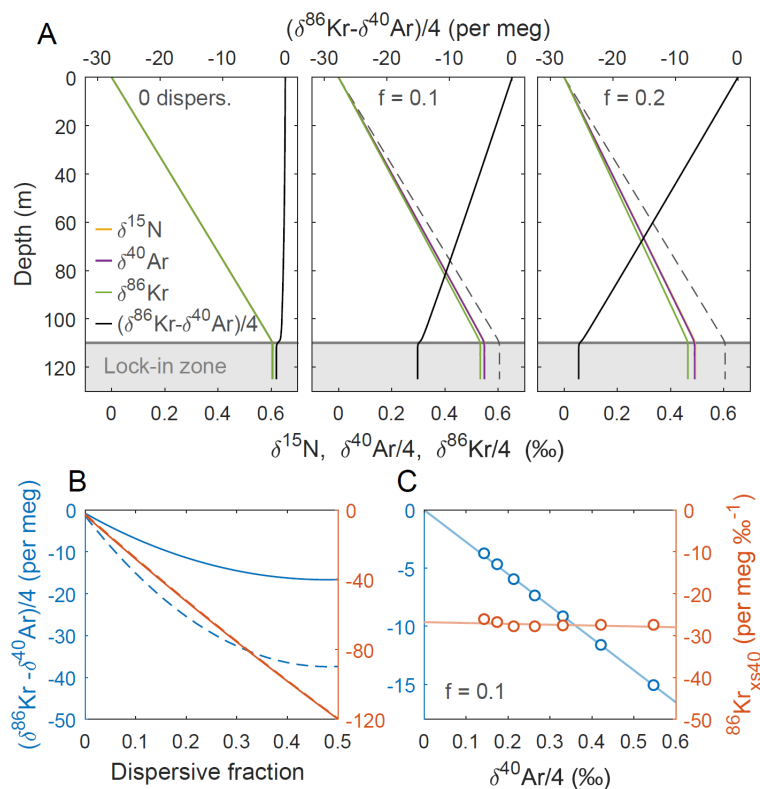
- 1031 Ikeda-Fukazawa, T., Fukumizu, K., Kawamura, K., Aoki, S., Nakazawa, T. and Hondoh, T. (2005) Effects of
1032 molecular diffusion on trapped gas composition in polar ice cores. *Earth Planet. Sci. Lett.* 229, 183-192.
- 1033 Kanner, L.C., Burns, S.J., Cheng, H. and Edwards, R.L. (2012) High-Latitude Forcing of the South American Summer
1034 Monsoon During the Last Glacial. *Science* 335, 570-573
- 1035 Kawamura, K., Severinghaus, J.P., Albert, M.R., Courville, Z.R., Fahnestock, M.A., Scambos, T., Shields, E. and
1036 Shuman, C.A. (2013) Kinetic fractionation of gases by deep air convection in polar firn. *Atmos. Chem. Phys.* 13,
1037 11141-11155.
- 1038 Kawamura, K., Severinghaus, J.P., Ishidoya, S., Sugawara, S., Hashida, G., Motoyama, H., Fujii, Y., Aoki, S. and
1039 Nakazawa, T. (2006) Convective mixing of air in firn at four polar sites. *Earth Planet. Sci. Lett.* 244, 672-682.
- 1040 Kobashi, T., Severinghaus, J.P. and Barnola, J.M. (2008a) 4 +/- 1.5 degrees C abrupt warming 11,270 yr ago identified
1041 from trapped air in Greenland ice. *Earth Planet. Sci. Lett.* 268, 397-407.
- 1042 Kobashi, T., Severinghaus, J.P. and Kawamura, K. (2008b) Argon and nitrogen isotopes of trapped air in the GISP2
1043 ice core during the Holocene epoch (0-11,500 B.P.): Methodology and implications for gas loss processes.
1044 *Geochim. Cosmochim. Acta* 72, 4675-4686.
- 1045 Kohfeld, K.E., Graham, R.M., de Boer, A.M., Sime, L.C., Wolff, E.W., Le Quéré, C. and Bopp, L. (2013) Southern
1046 Hemisphere westerly wind changes during the Last Glacial Maximum: paleo-data synthesis. *Quat. Sci. Rev.* 68,
1047 76-95.
- 1048 Koutavas, A., deMenocal, P.B., Olive, G.C. and Lynch-Stieglitz, J. (2006) Mid-Holocene El Niño–Southern
1049 Oscillation (ENSO) attenuation revealed by individual foraminifera in eastern tropical Pacific sediments. *Geology*
1050 34, 993-996.
- 1051 Koutavas, A., Lynch-Stieglitz, J., Marchitto, T.M. and Sachs, J.P. (2002) El Niño-Like Pattern in Ice Age Tropical
1052 Pacific Sea Surface Temperature. *Science* 297, 226-230.
- 1053 Lamy, F., Chiang, J.C.H., Martínez-Méndez, G., Thierens, M., Arz, H.W., Bosmans, J., Hebbeln, D., Lambert, F.,
1054 Lembke-Jene, L. and Stuut, J.-B. (2019) Precession modulation of the South Pacific westerly wind belt over the
1055 past million years. *Proc. Natl. Acad. Sci. U. S. A.*, 201905847.
- 1056 Lee, S. and Kim, H.-k. (2003) The Dynamical Relationship between Subtropical and Eddy-Driven Jets. *Journal of the*
1057 *Atmospheric Sciences* 60, 1490-1503.
- 1058 Lee, S.Y., Chiang, J.C., Matsumoto, K. and Tokos, K.S. (2011) Southern Ocean wind response to North Atlantic
1059 cooling and the rise in atmospheric CO₂: Modeling perspective and paleoceanographic implications.
1060 *Paleoceanography* 26.
- 1061 Liu, Z., Kutzbach, J. and Wu, L. (2000) Modeling climate shift of El Nino variability in the Holocene. *Geophys. Res.*
1062 *Lett.* 27, 2265-2268.
- 1063 Liu, Z., Lu, Z., Wen, X., Otto-Bliesner, B.L., Timmermann, A. and Cobb, K.M. (2014) Evolution and forcing
1064 mechanisms of El Nino over the past 21,000 years. *Nature* 515, 550-553.
- 1065 Lynch-Stieglitz, J. (2017) The Atlantic Meridional Overturning Circulation and Abrupt Climate Change. *Annual*
1066 *Review of Marine Science* 9, 83-104.
- 1067 Mantua, N.J. and Hare, S.R. (2002) The Pacific Decadal Oscillation. *Journal of Oceanography* 58, 35-44.
- 1068 Marcott, S.A., Shakun, J.D., Clark, P.U. and Mix, A.C. (2013) A Reconstruction of Regional and Global Temperature
1069 for the Past 11,300 Years. *Science* 339, 1198-1201.
- 1070 Marino, G., Zahn, R., Ziegler, M., Purcell, C., Knorr, G., Hall, I.R., Ziveri, P. and Elderfield, H. (2013) Agulhas salt-
1071 leakage oscillations during abrupt climate changes of the Late Pleistocene. *Paleoceanography* 28, 599-606.
- 1072 Markle, B.R., Steig, E.J., Buizert, C., Schoenemann, S.W., Bitz, C.M., Fudge, T.J., Pedro, J.B., Ding, Q., Jones, T.R.,
1073 White, J.W.C. and Sowers, T. (2017) Global atmospheric teleconnections during Dansgaard-Oeschger events.
1074 *Nature Geosci* 10, 36-40.
- 1075 Marshall, J. and Speer, K. (2012) Closure of the meridional overturning circulation through Southern Ocean
1076 upwelling. *Nature Geosci* 5, 171-180.
- 1077 McGee, D., Donohoe, A., Marshall, J. and Ferreira, D. (2014) Changes in ITCZ location and cross-equatorial heat
1078 transport at the Last Glacial Maximum, Heinrich Stadial 1, and the mid-Holocene. *Earth Planet. Sci. Lett.* 390, 69-
1079 79.
- 1080 Merkel, U., Prange, M. and Schulz, M. (2010) ENSO variability and teleconnections during glacial climates. *Quat.*
1081 *Sci. Rev.* 29, 86-100.
- 1082 Mo, K.C. and Paegle, J.N. (2001) The Pacific–South American modes and their downstream effects. *International*
1083 *Journal of Climatology* 21, 1211-1229.
- 1084 Moy, C.M., Seltzer, G.O., Rodbell, D.T. and Anderson, D.M. (2002) Variability of El Niño/Southern Oscillation
1085 activity at millennial timescales during the Holocene epoch. *Nature* 420, 162.



- 1086 Nakamura, H. and Shimpo, A. (2004) Seasonal Variations in the Southern Hemisphere Storm Tracks and Jet Streams
1087 as Revealed in a Reanalysis Dataset. *J. Clim.* 17, 1828-1844.
- 1088 Orsi, A.J., Kawamura, K., Fegyveresi, J.M., Headly, M.A., Alley, R.B. and Severinghaus, J.P. (2015) Differentiating
1089 bubble-free layers from melt layers in ice cores using noble gases. *J. Glaciol.* 61, 585-594.
- 1090 Oyabu, I., Kawamura, K., Uchida, T., Fujita, S., Kitamura, K., Hirabayashi, M., Aoki, S., Morimoto, S., Nakazawa,
1091 T., Severinghaus, J.P. and Morgan, J.D. (2021) Fractionation of O₂/N₂ and Ar/N₂ in the Antarctic ice sheet during
1092 bubble formation and bubble-clathrate hydrate transition from precise gas measurements of the Dome Fuji ice
1093 core. *The Cryosphere* 15, 5529-5555.
- 1094 Parkinson, C.L. and Cavalieri, D.J. (2012) Antarctic sea ice variability and trends, 1979–2010. *The Cryosphere*
1095 6, 871-880.
- 1096 Pedro, J.B., Jochum, M., Buizert, C., He, F., Barker, S. and Rasmussen, S.O. (2018) Beyond the bipolar seesaw:
1097 Toward a process understanding of interhemispheric coupling. *Quat. Sci. Rev.* 192, 27-46.
- 1098 Peterson, L.C., Haug, G.H., Hughen, K.A. and Röhl, U. (2000) Rapid Changes in the Hydrologic Cycle of the Tropical
1099 Atlantic During the Last Glacial. *Science* 290, 1947-1951.
- 1100 Rahmstorf, S. (2002) Ocean circulation and climate during the past 120,000 years. *Nature* 419, 207-214.
- 1101 Raynaud, D., Lipenkov, V., Lemieux-Dudon, B., Duval, P., Loutre, M.F. and Lhomme, N. (2007) The local insolation
1102 signature of air content in Antarctic ice. A new step toward an absolute dating of ice records. *Earth Planet. Sci.*
1103 *Lett.* 261, 337-349.
- 1104 Rein, B., Lückge, A., Reinhardt, L., Sirocko, F., Wolf, A. and Dullo, W.-C. (2005) El Niño variability off Peru during
1105 the last 20,000 years. *Paleoceanography* 20.
- 1106 Rhodes, R.H., Faïn, X., Brook, E.J., McConnell, J.R., Maselli, O.J., Sigl, M., Edwards, J., Buizert, C., Blunier, T.,
1107 Chappellaz, J. and Freitag, J. (2016) Local artifacts in ice core methane records caused by layered bubble trapping
1108 and in situ production: a multi-site investigation. *Clim. Past* 12, 1061-1077.
- 1109 Riedinger, M.A., Steinitz-Kannan, M., Last, W.M. and Brenner, M. (2002) A ~6100 14C yr record of El Niño activity
1110 from the Galápagos Islands. *Journal of Paleolimnology* 27, 1-7.
- 1111 Rind, D., Russell, G., Schmidt, G., Sheth, S., Collins, D., Demenocal, P. and Teller, J. (2001) Effects of glacial
1112 meltwater in the GISS coupled atmosphere-ocean model: 2. A bipolar seesaw in Atlantic Deep Water production.
1113 *Journal of Geophysical Research: Atmospheres* (1984–2012) 106, 27355-27365.
- 1114 Rojas, M., Moreno, P., Kageyama, M., Crucifix, M., Hewitt, C., Abe-Ouchi, A., Ohgaito, R., Brady, E.C. and Hope,
1115 P. (2009) The Southern Westerlies during the last glacial maximum in PMIP2 simulations. *Clim. Dyn.* 32, 525-
1116 548.
- 1117 Russell, J.L., Dixon, K.W., Gnanadesikan, A., Stouffer, R.J. and Toggweiler, J.R. (2006) The Southern Hemisphere
1118 Westerlies in a Warming World: Propping Open the Door to the Deep Ocean. *J. Clim.* 19, 6382-6390.
- 1119 Sadekov, A.Y., Ganeshram, R., Pichevin, L., Berdin, R., McClymont, E., Elderfield, H. and Tudhope, A.W. (2013)
1120 Palaeoclimate reconstructions reveal a strong link between El Niño-Southern Oscillation and Tropical Pacific mean
1121 state. *Nature Communications* 4, 2692.
- 1122 Salau, O., Schneider, B., Park, W., Khon, V. and Latif, M. (2012) Modeling the ENSO impact of orbitally induced
1123 mean state climate changes. *J. Geophys. Res.* 117.
- 1124 Schaller, C.F., Freitag, J. and Eisen, O. (2017) Critical porosity of gas enclosure in polar firn independent of climate.
1125 *Clim. Past* 13, 1685-1693.
- 1126 Schneider, T., Bischoff, T. and Haug, G.H. (2014) Migrations and dynamics of the intertropical convergence zone.
1127 *Nature* 513, 45-53.
- 1128 Schwander, J. (1989) The transformation of snow to ice and the occlusion of gases in: Oescher, H., Langway, C.C.
1129 (Eds.), *The Environmental record in glaciers and ice sheets*. John Wiley, New York, pp. 53-67.
- 1130 Schwander, J., Barnola, J.M., Andrie, C., Leuenberger, M., Ludin, A., Raynaud, D. and Stauffer, B. (1993) THE AGE
1131 OF THE AIR IN THE FIRN AND THE ICE AT SUMMIT, GREENLAND. *J. Geophys. Res.* 98, 2831-2838.
- 1132 Schwander, J., Stauffer, B. and Sigg, A. (1988) Air mixing in firn and the age of the air at pore close-off, *Annals of*
1133 *Glaciology*, pp. 141-145.
- 1134 Severinghaus, J.P., Albert, M.R., Courville, Z.R., Fahnstock, M.A., Kawamura, K., Montzka, S.A., Muhle, J.,
1135 Scambos, T.A., Shields, E., Shuman, C.A., Suwa, M., Tans, P. and Weiss, R.F. (2010) Deep air convection in the
1136 firn at a zero-accumulation site, central Antarctica. *Earth Planet. Sci. Lett.* 293, 359-367.
- 1137 Severinghaus, J.P. and Battle, M.O. (2006) Fractionation of gases in polar ice during bubble close-off: New constraints
1138 from firn air Ne, Kr and Xe observations. *Earth Planet. Sci. Lett.* 244, 474-500.
- 1139 Severinghaus, J.P., Beaudette, R., Headly, M.A., Taylor, K. and Brook, E.J. (2009) Oxygen-18 of O₂ Records the
1140 Impact of Abrupt Climate Change on the Terrestrial Biosphere. *Science* 324, 1431-1434.

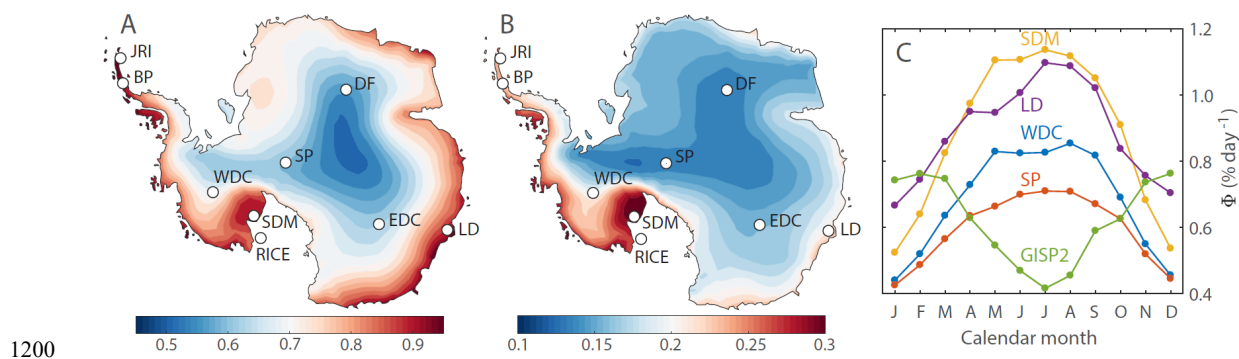


- 1141 Severinghaus, J.P., Grachev, A., Luz, B. and Caillon, N. (2003) A method for precise measurement of argon 40/36
1142 and krypton/argon ratios in trapped air in polar ice with applications to past firn thickness and abrupt climate
1143 change in Greenland and at Siple Dome, Antarctica. *Geochim. Cosmochim. Acta* 67, 325-343.
- 1144 Severinghaus, J.P., Sowers, T., Brook, E.J., Alley, R.B. and Bender, M.L. (1998) Timing of abrupt climate change at
1145 the end of the Younger Dryas interval from thermally fractionated gases in polar ice. *Nature* 391, 141-146.
- 1146 Shakun, J.D., Clark, P.U., He, F., Marcott, S.A., Mix, A.C., Liu, Z., Otto-Bliesner, B., Schmittner, A. and Bard, E.
1147 (2012) Global warming preceded by increasing carbon dioxide concentrations during the last deglaciation. *Nature*
1148 484, 49-54.
- 1149 Sime, L.C., Kohfeld, K.E., Le Quéré, C., Wolff, E.W., de Boer, A.M., Graham, R.M. and Bopp, L. (2013) Southern
1150 Hemisphere westerly wind changes during the Last Glacial Maximum: model-data comparison. *Quat. Sci. Rev.*
1151 64, 104-120.
- 1152 Simpson, I.R., Hitchcock, P., Shepherd, T.G. and Scinocca, J.F. (2011) Stratospheric variability and tropospheric
1153 annular-mode timescales. *Geophys. Res. Lett.* 38.
- 1154 Sowers, T., Bender, M., Raynaud, D. and Korotkevich, Y.S. (1992) $\delta^{15}\text{N}$ of N_2 in air trapped in polar ice: A tracer
1155 of gas transport in the firn and a possible constraint on ice age-gas age differences. *J. Geophys. Res.* 97, 15683-
1156 15697.
- 1157 Stott, L., Poulsen, C., Lund, S. and Thunell, R. (2002) Super ENSO and Global Climate Oscillations at Millennial
1158 Time Scales. *Science* 297, 222-226.
- 1159 Studer, A.S., Sigman, D.M., Martínez-García, A., Benz, V., Winckler, G., Kuhn, G., Esper, O., Lamy, F., Jaccard,
1160 S.L., Wacker, L., Oleynik, S., Gersonde, R. and Haug, G.H. (2015) Antarctic Zone nutrient conditions during the
1161 last two glacial cycles. *Paleoceanography* 30, 2014PA002745.
- 1162 Studer, A.S., Sigman, D.M., Martínez-García, A., Thöle, L.M., Michel, E., Jaccard, S.L., Lippold, J.A., Mazaud, A.,
1163 Wang, X.T., Robinson, L.F., Adkins, J.F. and Haug, G.H. (2018) Increased nutrient supply to the Southern Ocean
1164 during the Holocene and its implications for the pre-industrial atmospheric CO_2 rise. *Nat. Geosci.* 11, 756-760.
- 1165 Thomas, E.R., Marshall, G.J. and McConnell, J.R. (2008) A doubling in snow accumulation in the western Antarctic
1166 Peninsula since 1850. *Geophys. Res. Lett.* 35.
- 1167 Thompson, D.W.J. and Wallace, J.M. (2000) Annular Modes in the Extratropical Circulation. Part I: Month-to-Month
1168 Variability*. *J. Clim.* 13, 1000-1016.
- 1169 Thompson, L.G., Mosley-Thompson, E., Davis, M.E., Zagorodnov, V.S., Howat, I.M., Mikhailenko, V.N. and Lin, P.-
1170 N. (2013) Annually Resolved Ice Core Records of Tropical Climate Variability over the Past ~1800 Years. *Science*
1171 340, 945-950.
- 1172 Timmermann, A., Okumura, Y., An, S.I., Clement, A., Dong, B., Guilyardi, E., Hu, A., Jungclauss, J.H., Renold, M.,
1173 Stocker, T.F., Stouffer, R.J., Sutton, R., Xie, S.P. and Yin, J. (2007) The Influence of a Weakening of the Atlantic
1174 Meridional Overturning Circulation on ENSO. *J. Clim.* 20, 4899-4919.
- 1175 Toggweiler, J.R., Russell, J.L. and Carson, S.R. (2006) Midlatitude westerlies, atmospheric CO_2 , and climate change
1176 during the ice ages. *Paleoceanography* 21, PA2005.
- 1177 Trenberth, K.E. (1991) Storm Tracks in the Southern Hemisphere. *Journal of the Atmospheric Sciences* 48, 2159-
1178 2178.
- 1179 Tudhope, A.W., Chilcott, C.P., McCulloch, M.T., Cook, E.R., Chappell, J., Ellam, R.M., Lea, D.W., Lough, J.M. and
1180 Shimmield, G.B. (2001) Variability in the El Niño-Southern Oscillation through a glacial-interglacial cycle.
1181 *Science* 291, 1511-1517.
- 1182 Wang, X., Auler, A.S., Edwards, R.L., Cheng, H., Ito, E., Wang, Y., Kong, X. and Solheid, M. (2007) Millennial-
1183 scale precipitation changes in southern Brazil over the past 90,000 years. *Geophys. Res. Lett.* 34.
- 1184 Wang, Y.J., Cheng, H., Edwards, R.L., An, Z.S., Wu, J.Y., Shen, C.C. and Dorale, J.A. (2001) A High-Resolution
1185 Absolute-Dated Late Pleistocene Monsoon Record from Hulu Cave, China. *Science* 294, 2345-2348.
- 1186 Zheng, W., Braconnot, P., Guilyardi, E., Merkel, U. and Yu, Y. (2008) ENSO at 6ka and 21ka from ocean-atmosphere
1187 coupled model simulations. *Clim. Dyn.* 30, 745-762.



1188

1189 **Figure 1.** Idealized firn air transport model experiments of $^{86}\text{Kr}_{\text{xs}}$. Firn density is calculated using (Herron
 1190 and Langway, 1980), and the diffusivity using (Schwander, 1989). **A** Simulations using a fraction of
 1191 dispersive mixing of $f=0$ (left), $f=0.1$ (middle) and $f=0.2$ (right) for a hypothetical site with accumulation
 1192 rate of $A = 2 \text{ cm a}^{-1}$ ice equivalent and mean annual temperature $T = -60^\circ\text{C}$. At dispersive fraction f , effective
 1193 molecular diffusivity of all gases is multiplied by $(1-f)$ and dispersive mixing for all gases is set equal to f
 1194 times the effective molecular diffusivity of CO_2 . **B** Isotopic disequilibrium as a function of dispersive
 1195 mixing intensity at two different firn thicknesses of around 100 m (dashed, $A = 2 \text{ cm a}^{-1}$ and $T = -60^\circ\text{C}$) and
 1196 50 m (solid, $A = 2 \text{ cm a}^{-1}$ and $T = -43^\circ\text{C}$). We compare isotopic disequilibrium without (blue, left axis) and
 1197 with (orange, right axis) normalization. **C** Simulations at 10 % dispersive mixing, where each dot represents
 1198 different climatic conditions. Accumulation rate is $A = 2 \text{ cm a}^{-1}$ ice equivalent and mean annual temperature
 1199 is changed from -60°C to -30°C in steps of 5°C .



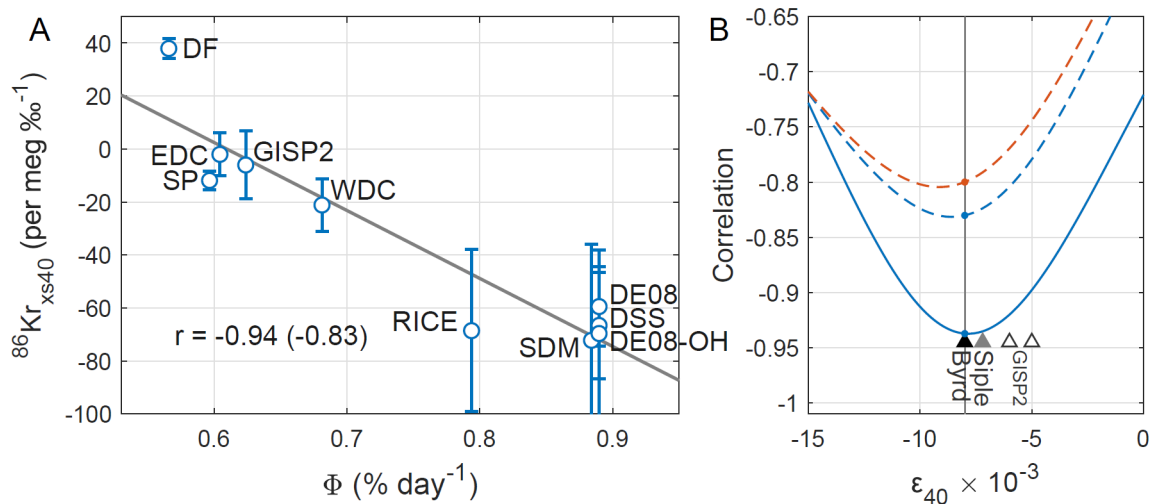
1200

1201

1202 **Figure 2.** Calibrating Kr-86 excess. **A** Annual-mean Φ in Antarctica over 1979-2017, in units of $\% \text{ day}^{-1}$.

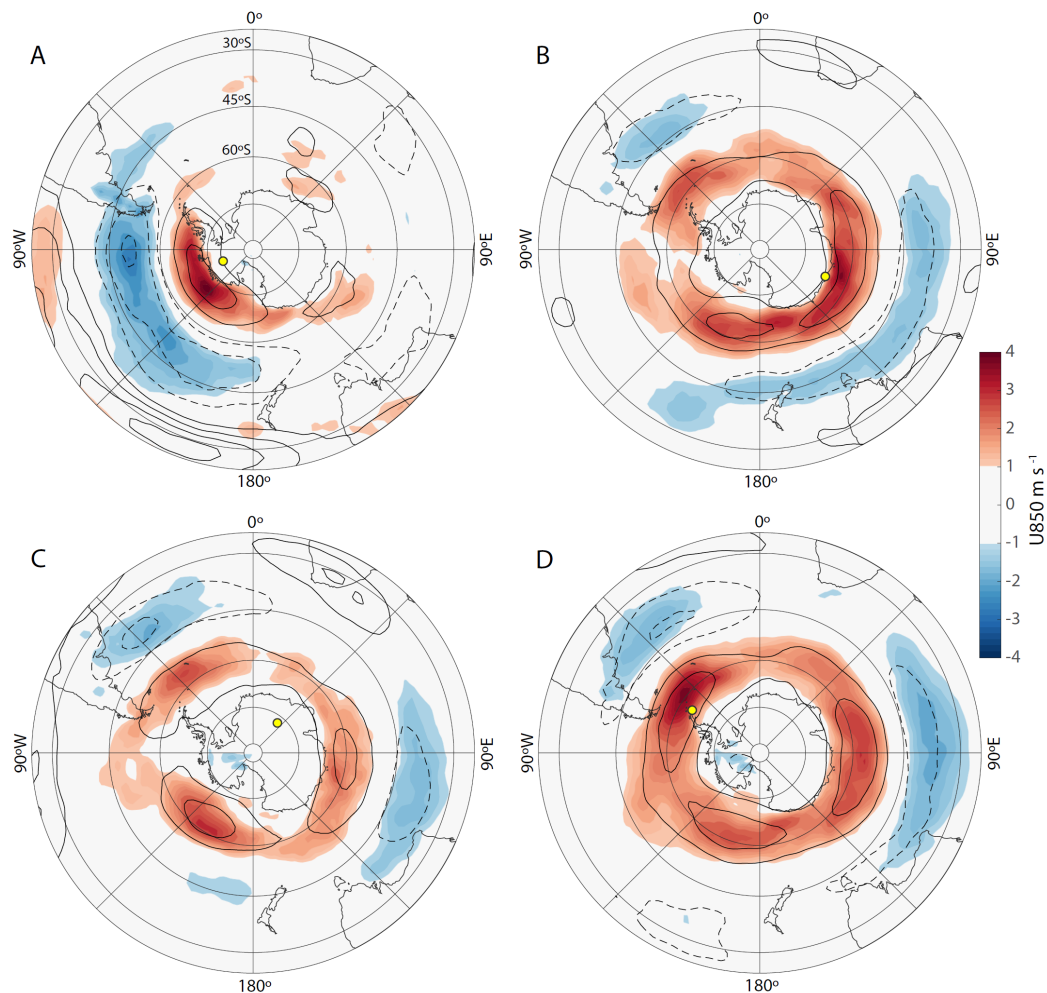
1203 **B** Interannual variability (1σ standard deviation) of annual-mean Φ over 1979-2017, in units of $\% \text{ day}^{-1}$. **C**

1204 Annual cycle in Φ for 1979-2017 for the indicated sites.



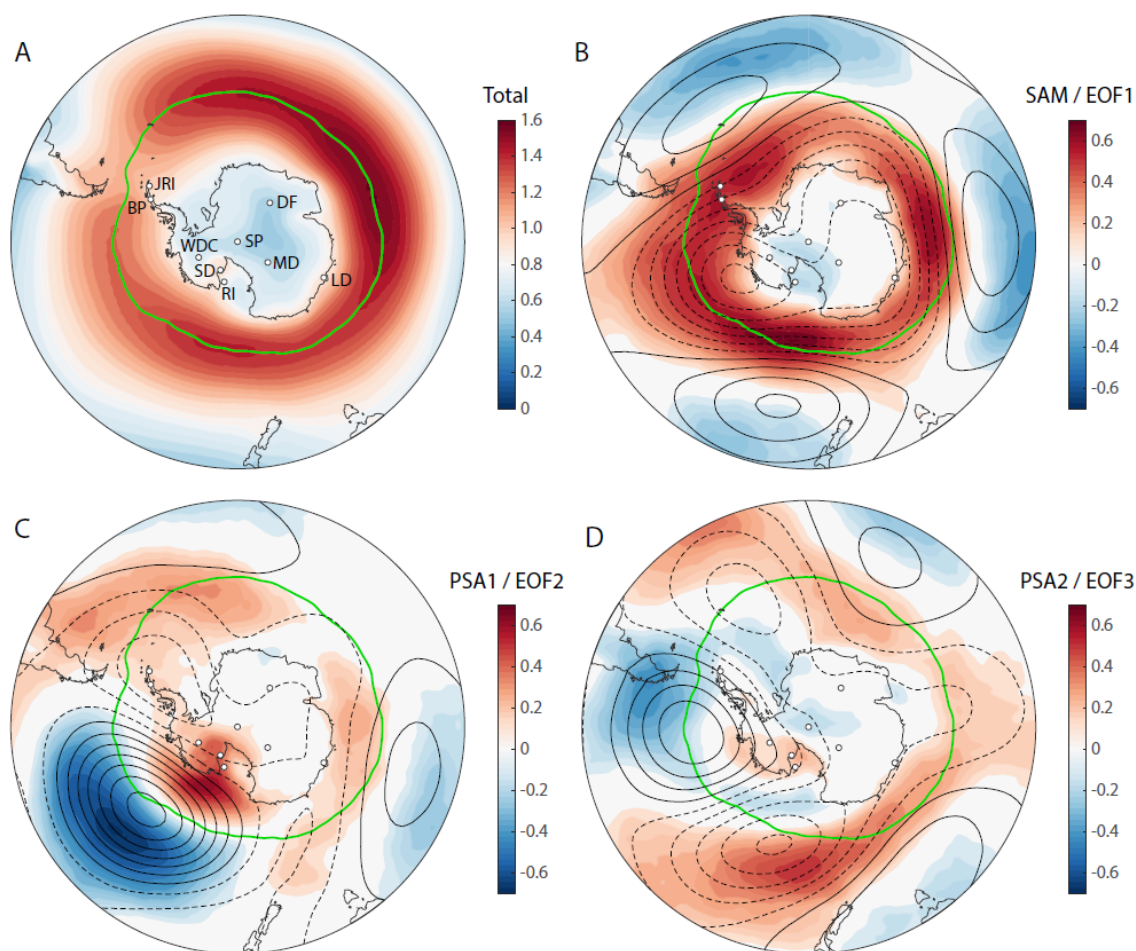
1205

1206 **Figure 3.** Calibrating Kr-86 excess. **A** $^{86}\text{Kr}_{\text{xs}}$ as a function of Φ for the calibration data set. Circles give the
 1207 site mean, and the error bars denote the $\pm 1\sigma$ standard deviation between samples (uncertainty in corrections
 1208 not included). Pearson correlation coefficient is $r = -0.94$ when considering site data means and $r = -0.83$
 1209 when considering all individual samples. Data are corrected for gas loss using $\epsilon_{40} = -0.008$ (Appendix A1),
 1210 and corrected for thermal fractionation using site-mean N-15 excess (Appendix A2). The calibration curve
 1211 for $^{86}\text{Kr}_{\text{xs}15}$ is identical in this case, with slightly larger errorbars. **B** Correlation of the calibration curve as
 1212 a function of the gas loss correction scaling parameter ϵ_{40} . The solid line gives the correlation for both site-
 1213 mean $^{86}\text{Kr}_{\text{xs}15}$ and $^{86}\text{Kr}_{\text{xs}40}$ (identical); the dashed lines the correlation using individual samples for $^{86}\text{Kr}_{\text{xs}40}$
 1214 (blue) and $^{86}\text{Kr}_{\text{xs}15}$ (orange). Triangles denote the ϵ_{40} estimate from the Byrd, Siple and GISP2 ice cores
 1215 (Fig. A2; Kobashi et al., 2008a; Severinghaus et al., 2003).



1216

1217 **Figure 4.** Zonal wind speed at 850 hPa (color shading, see scale bar) and 200 hPa (2 m s^{-1} contours)
1218 regressed onto surface synoptic activity Φ at the Antarctic ice core sites of: **A** WAIS Divide; **B** Law
1219 Dome (DE08, DE08-OH and DSSW20K); **C** Dome Fuji; **D** James Ross Island. Yellow dots mark the ice
1220 core locations.

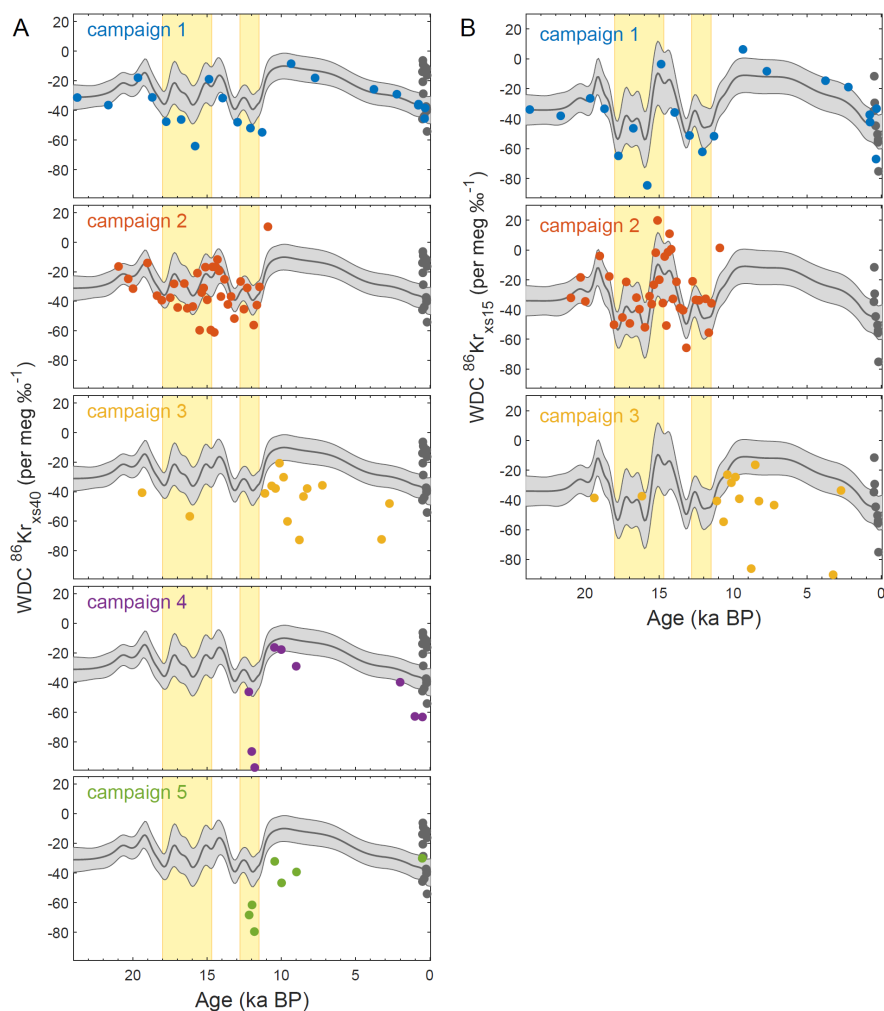


1221

1222 **Figure 5.** Modes of SH extratropical atmospheric variability and their link to synoptic-scale surface
1223 pressure variability in Antarctica. **A** Annual mean Φ in units of $\% \text{ day}^{-1}$; latitude of maximum Φ denoted
1224 by green line. **B** Colors show correlation between Φ and the Southern Annular Mode (SAM) index, with
1225 superimposed the 500 hPa geopotential height anomalies in 10 m contours. **C** as panel B, but for the Pacific-
1226 South American Pattern 1 (PSA1). **D** As panel B, but for the Pacific-South American Pattern 2 (PSA2).
1227 SAM, PSA1 and PSA2 are defined as respectively the first, second and third EOFs (Empirical Orthogonal
1228 Functions) of the 500 hPa geopotential height anomalies in 20° - 90° S monthly values in the 1979-2017 ERA
1229 interim reanalysis (Dee et al., 2011).



1230



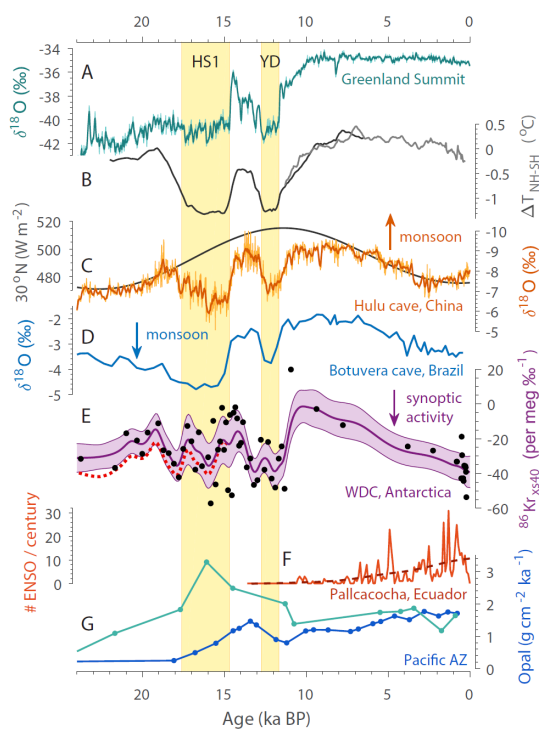
1231

1232

1233 **Figure 6.** WAIS Divide Kr-86 excess records through the last deglaciation. **A** WDC $^{86}\text{Kr}_{\text{xs40}}$ data from the
1234 five measurement campaigns. The gray curve shows a Gaussian smoothing curve to the combined data
1235 from the first two campaigns; the light gray shaded area shows the $\pm 1\sigma$ uncertainty envelope based on a
1236 10,000 iteration Monte-Carlo sampling of the errors and uncertainties. The WDC calibration data is shown
1237 as gray circles for comparison. **B** As in panel (A), but for $^{86}\text{Kr}_{\text{xs15}}$. For campaigns 4 and 5 the sample was
1238 not split, and no $\delta^{15}\text{N}$ data are available. The Heinrich Stadial 1 and Younger Dryas North-Atlantic cold
1239 periods marked in yellow.

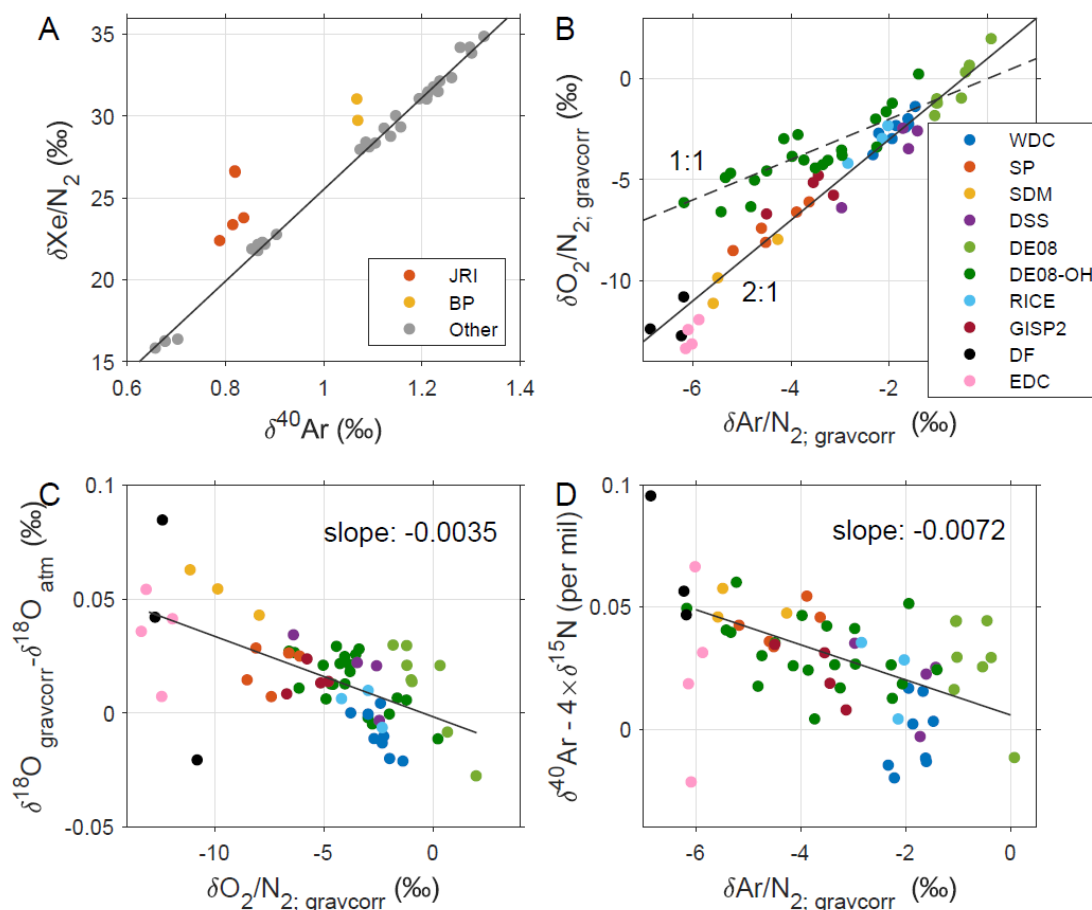


1240



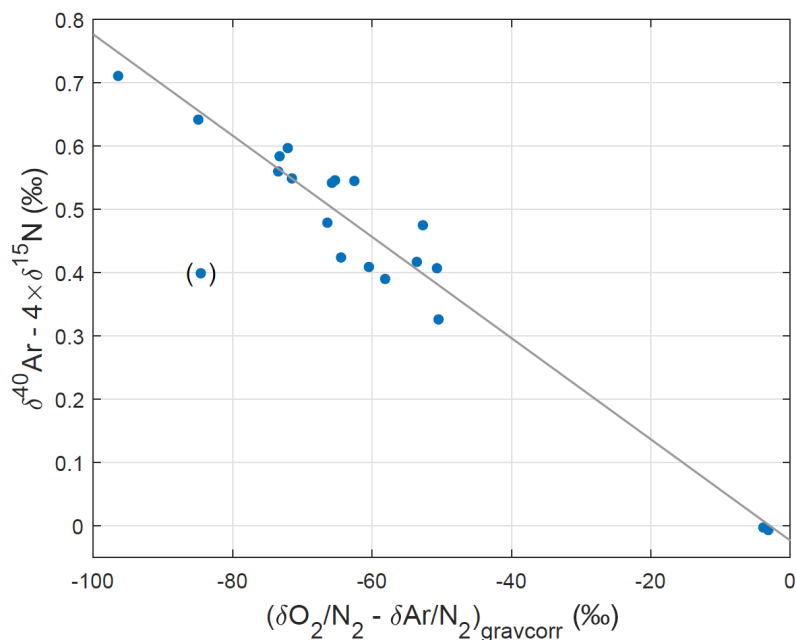
1241

1242 **Figure 7.** Climate records through the last deglaciation with the Heinrich Stadial 1 (HS1) and Younger
1243 Dryas (YD) North-Atlantic cold periods marked in yellow. **A** Greenland Summit ice core stable water
1244 isotope ratio $\delta^{18}\text{O}$ here the average of the GISP2 and GRIP ice cores (Grootes et al., 1993). **B** Hemispheric
1245 temperature difference (McGee et al., 2014) based on global proxy compilations for the Holocene (Marcott
1246 et al., 2013) and last deglaciation (Shakun et al., 2012). **C** Speleothem calcite $\delta^{18}\text{O}$ from Hulu and Dongge
1247 Caves, China, as a proxy for East Asian summer monsoon strength (Dykoski et al., 2005; Wang et al.,
1248 2001). Superimposed is summer solstice (June 21) insolation at 30°N . **D** Speleothem calcite $\delta^{18}\text{O}$ from
1249 Botuvera cave, southern Brazil, as a proxy for South American summer monsoon strength (Cruz et al.,
1250 2005; Wang et al., 2007). **E** Kr-86 excess record from WAIS Divide (this study); corrected for gas loss and
1251 thermal fractionation (Appendix A). Center line and shaded envelope show the mean and $\pm 1\sigma$ uncertainty
1252 interval of a 10,000 iteration Monte Carlo smoothing exercise (see text). The dotted red line equals the
1253 center line with a correction for elevation change applied (Appendix A) using a simulated elevation history
1254 (Golledge et al., 2014). **F** Number of El Niño events per century from laminations in sediments from Laguna
1255 Pallcacocha, Ecuador (Moy et al., 2002). **G** Th-normalized opal flux in the Pacific Antarctic zone (south of
1256 the polar front) from cores NBP9802-6PC1 (turquoise; 169.98°W , 61.88°S) and PS75/072-4 (blue;
1257 151.22°W , 57.56°S), reflecting local productivity and (wind-driven) upwelling (Chase et al., 2003; Studer
1258 et al., 2015). All isotope data in this figure are on the V-SMOW scale. Arrows show direction of increased
1259 monsoon strength / synoptic activity.



1260

1261 **Figure A1.** Elemental ratios in the 11-site calibration study of late Holocene samples. **A** $\delta\text{Xe}/\text{N}_2$ vs. $\delta^{40}\text{Ar}$
 1262 in all ice core samples. $\delta^{40}\text{Ar}$ is used solely to illustrate gravitational enrichment, and a similar picture arises
 1263 when plotted against any isotopic pair. Refrozen meltwater (elevated $\delta\text{Xe}/\text{N}_2$) was seen in all samples from
 1264 the Antarctic Peninsula (James Ross Island and Bruce Plateau sites), despite selecting samples free of
 1265 visible melt features. **B** The relationship between the commonly used gas loss proxies $\delta\text{O}_2/\text{N}_2$ and $\delta\text{Ar}/\text{N}_2$
 1266 corrected for gravity. **C** Enrichment in $\delta^{18}\text{O}$ (corrected for gravity and atmospheric $\delta^{18}\text{O}_{\text{atm}}$) plotted against
 1267 gravity-corrected $\delta\text{O}_2/\text{N}_2$ **D** $\delta^{40}\text{Ar}$ enrichment plotted against gravity-corrected $\delta\text{Ar}/\text{N}_2$. In all panels
 1268 gravitational correction is applied by subtracting $\delta^{15}\text{N}$ times the atomic mass unit difference.

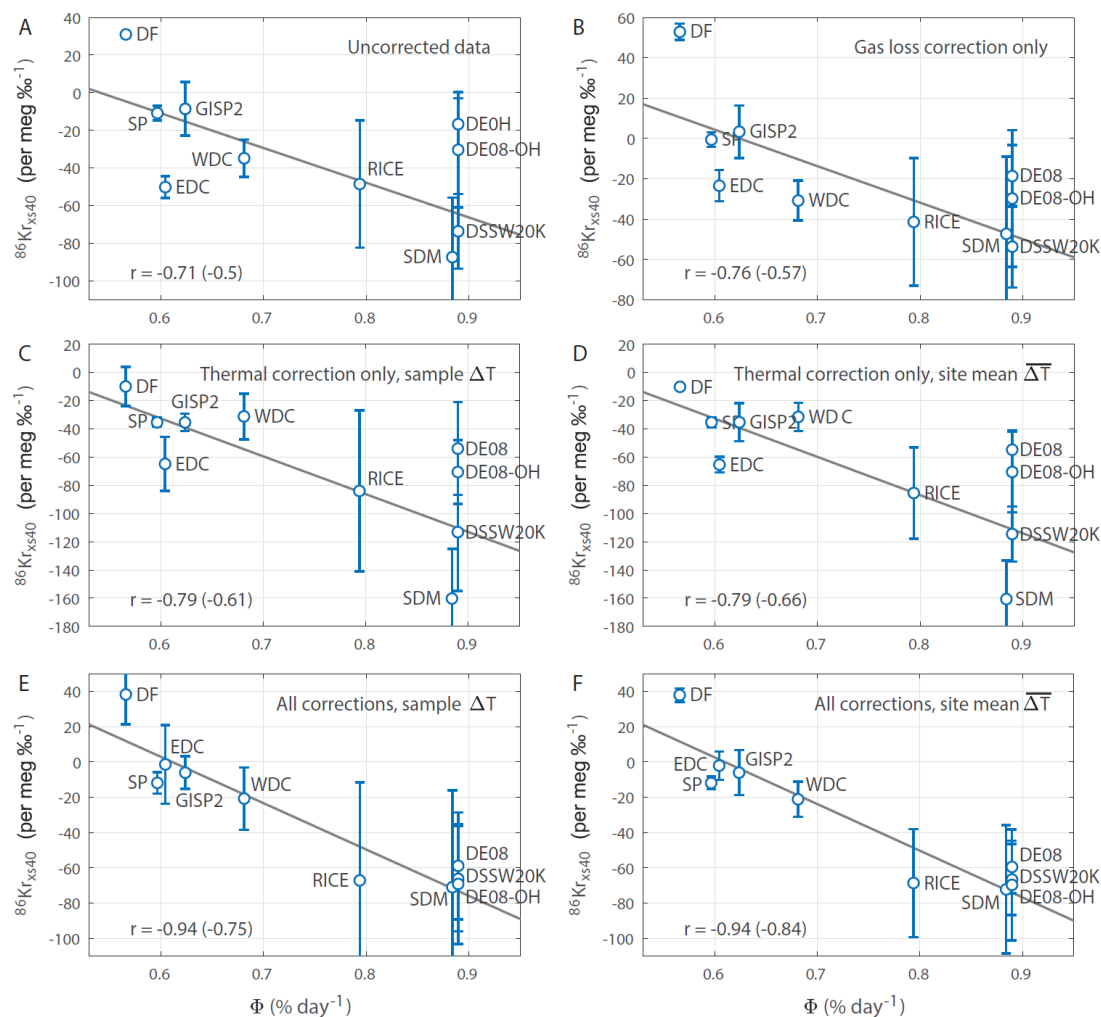


1269

1270 **Figure A2.** Argon isotopic enrichment due to gas loss. The enrichment in $\delta^{40}\text{Ar}$ plotted as a function of
1271 gravitationally corrected $(\delta\text{O}_2/\text{N}_2 - \delta\text{Ar}/\text{N}_2)_{\text{gravcorr}}$ measured in the deep Antarctic Byrd ice core, which suffered
1272 heavy gas loss. Ice samples were analyzed in the Bender Lab at the University of Rhode Island by Jeff
1273 Severinghaus in 1997. The slope of the least-square fit is $\epsilon_{40} = -0.008$. The data point in parentheses is
1274 treated as an outlier and excluded from the fitting.



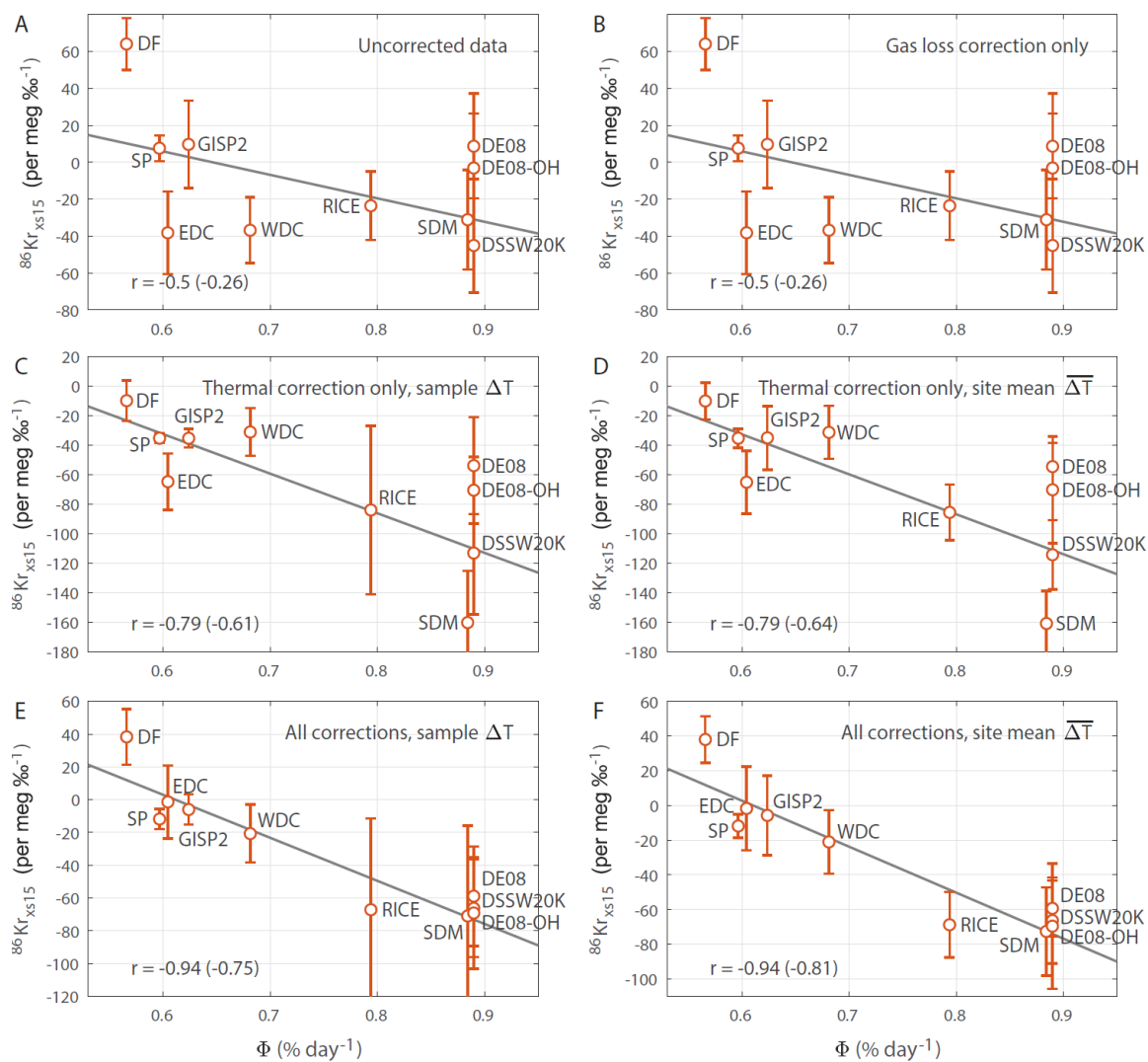
1275



1276

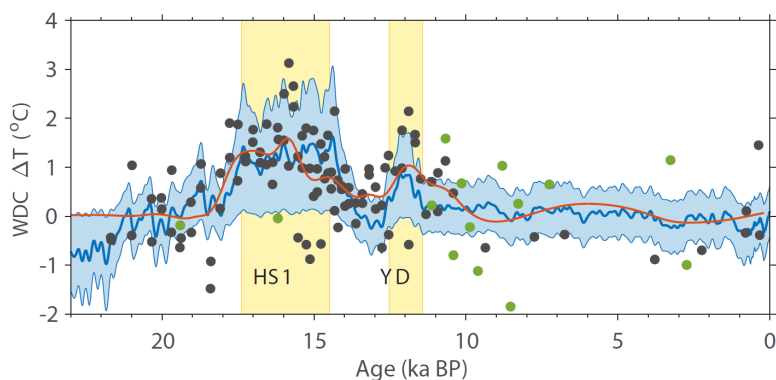
1277

1278 **Figure A3.** Influence of gas loss and thermal correction on the $^{86}\text{Kr}_{\text{xs40}}$ calibration. We plot $^{86}\text{Kr}_{\text{xs40}}$ as a
 1279 function of Φ **A** without any data corrections applied; **B** with only the gas loss correction applied ($\epsilon_{40} = -$
 1280 0.008); **C** with only the thermal correction applied using individual sample ΔT ; **D** with only the thermal
 1281 correction applied using individual site mean $\overline{\Delta T}$; **E** with both gas loss and thermal corrections applied
 1282 using individual sample ΔT ; **F** with both gas loss and thermal corrections applied using site mean $\overline{\Delta T}$. In
 1283 each panel the correlation to Φ are listed for the site-average and individual sample with the latter in
 1284 parentheses. For all correlations $p < 0.05$.



1285

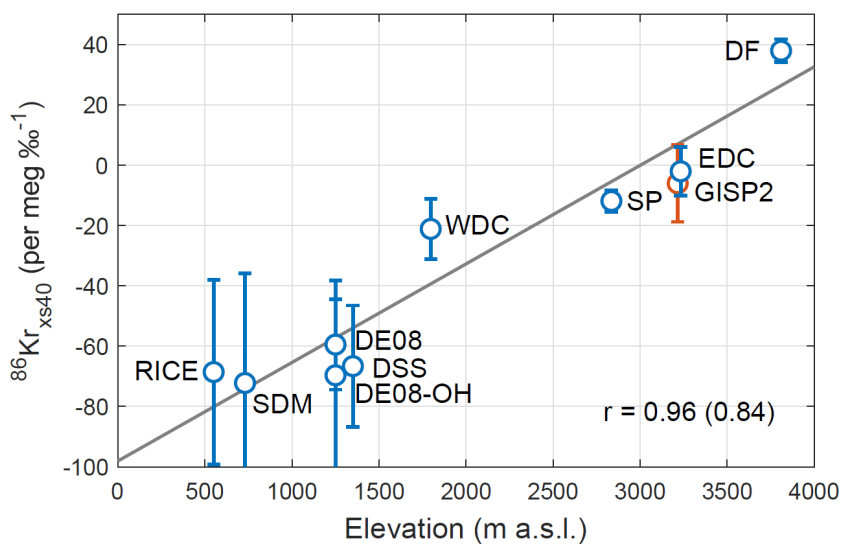
1286 **Figure A4.** Same as figure A3, but for $^{86}\text{Kr}_{\text{xs15}}$. Note that the gas loss correction (panel B) does not impact
 1287 $^{86}\text{Kr}_{\text{xs15}}$. For all correlations $p < 0.05$, except for panels A and B where $p = 0.16$ for the site-average
 1288 correlation.



1289

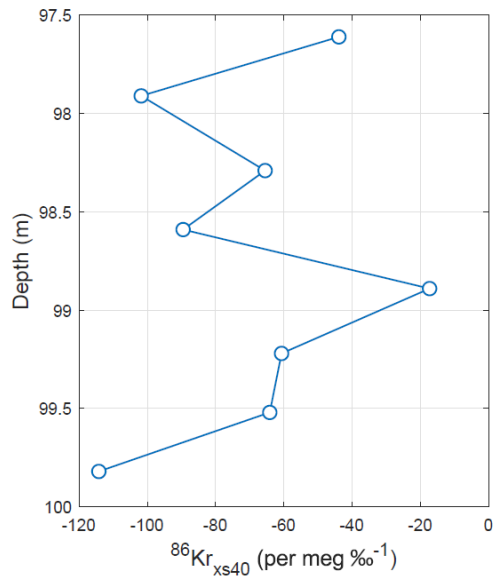
1290 **Figure A5.** The ΔT correction applied to the downcore records. Blue envelope shows the $\pm 2\sigma$ range of
1291 thermal correction scenarios in the Monte Carlo sampling, together with the mean (blue line). Gray dots
1292 show WDC ΔT estimates from available ^{15}N -excess data, with the red curve being a Gaussian smoothing
1293 function to the data. Green dots are ^{15}N -excess from campaign 3, showing somewhat greater scatter.

1294



1295

1296 **Figure A6.** Kr-86 excess dependence on site elevation. Vertical axis is the $^{86}\text{Kr}_{\text{xs}}$. The linear fit has a slope
1297 of 34 per meg ‰^{-1} per 1000 m elevation.



1298

1299 **Figure B1** High-resolution sub-annual sampling of $^{86}\text{Kr}_{\text{xs40}}$ in the DE08-OH site. The annual layer thickness
1300 at this depth is around 1.3 m.



1301 **Table 1.** Ice core sites used in this study, with N the number of samples included in the calibration study.
 1302 See the main text for acronyms.
 1303

Site	T (°C)	A (m ice a ⁻¹)	Φ (% day ⁻¹)	Latitude	Longitude	N
WDC	-31	0.22	0.68	79.5°S	112.1°W	8 ^a
DF	-57	0.028	0.56	77.3°S	39.7°E	3
SP	-51	0.078	0.6	90.0°S	98.2°W	5
SDM	-25	0.13	0.88	81.7°S	149.1°W	3
DSSW20K	-21	0.16	0.89	66.8°S	112.6°E	4
DE08	-19	1.2	0.89	66.7°S	113.2°E	8
DE08-OH	-19	1.2	0.89	66.7°S	113.2°E	8 ^b
RICE	-24	0.24	0.79	79.4°S	161.7°W	3 ^a
EDC	-55	0.03	0.6	75.1°S	123.4°E	4
JRI	-14	0.68	0.97	64.2°S	57.7°W	5 ^c
BP	-15	2	0.9	66.1°S	64.1°W	2 ^c
GISP2	-32	0.23	0.62	72.6°N	38.5°W	4

1304 ^a Not including one sample rejected due to technical problems.
 1305 ^b Only shallow samples due to strong gas loss in deeper samples attributed to warm storage conditions.
 1306 ^c Refrozen meltwater present as indicated by elevated Xe/N₂ ratio.
 1307
 1308
 1309
 1310

1311 **Table 2.** Pearson correlation between Φ at the ice coring sites and large-scale atmospheric circulation.
 1312 Correlations are calculated using annual mean data (all months, April-March). We only list the
 1313 statistically significant correlations ($p < 0.1$). The Niño 3.4 is calculated over 5°S - 5°N, 190°E - 240°E,
 1314 using SST from Huang et al. (2014); the PDO index is from Mantua and Hare (2002).
 1315

Site	SAM	PSA1	PSA2	Niño 3.4	PDO	Sea ice Am-Bell	Sea ice Ross
WDC	-	0.31	-	0.31	0.28	-	-
SDM	-	0.47	0.34	0.43	0.45	-	-0.32
RICE	-	0.41	0.34	0.34	0.45	-	-0.30
SP	-	-	-0.32	-	-0.30	-	-
LD	0.45	-	-	-	-	-	-
DF	0.37	-	-	-	-	-	-
EDC	0.30	-	-	-	-	-	-
JRI	0.67	-	-	-	-	0.31	-
BP	0.68	-	-	-	-	-	-

1316
 1317
 1318